

GPU-First Heisenberg-Picture Tensor Network Dynamics for the 2D Transverse-Field Ising Model

Paolo D’Alberto*
Advanced Micro Devices, Inc.
paolo.dalberto@amd.com

July 1, 2026

Abstract

We present CPPSIM, a C++/GPU 2D Ising simulator for Heisenberg-picture tensor network time evolution on GPUs. The key computational contributions are: first, a zero-alloc GPU workspace that pre-allocates all buffers at startup; second, a custom GPU tensor permutation kernel replacing host-side index shuffling with a pure device-to-device operation, yielding a 7.6× trotter speedup; third, a hybrid QR strategy selecting Cholesky-QR for tall-skinny matrices and Householder-QR otherwise; fourth, adaptive Belief Propagation with log-space Bethe partition function evaluation and explicit sign tracking. The key validation contributions are: first, correctness and demonstration of χ -convergence of the spin autocorrelation function $C(t)$ for $\chi \in \{20, \dots, 110\}$ on a 4×4 grid, identifying $\chi^* \approx 60$ as the practical convergence point. Second, we characterize BP fixed-point multiplicity and introduce a four-step trap remediation procedure using damped BP updates. Third, we identify operator-placement C_4 symmetry as the root cause of BP fixed-point multiplicity — symmetric grids are entirely trap-free. Fourth, grid scaling from 3×3 to 10×10 demonstrates operator lightcone saturation consistent with the Lieb–Robinson bound. A study across two 32 GB GPU configurations reveals complementary BP trap patterns and defines portable operating points at $\chi \in \{40, 60\}$. An analytic memory model, validated to within 2% against hardware measurements, guided deployment on a 192+ GB configuration, where we demonstrate the first tensor-network simulation of the 2D Ising model on a 10×10 lattice at $\chi_{\max} = 100$ (≈ 109 GB) and an 11×11 lattice at $\chi_{\max} = 100$ (≈ 130 GB). The 11×11 C_4 -symmetric run is entirely trap-free and reveals a clean three-phase operator spreading: ballistic Lieb–Robinson cone, boundary reflection ring, and onset of full scrambling.

1 Introduction

Simulating real-time quantum dynamics of strongly correlated many-body systems is a central challenge in computational physics. Tensor network (TN) methods provide a systematically improvable approximation by representing quantum operators as networks of low-rank tensors [1], with accuracy controlled by the bond dimension χ . While one-dimensional systems are well-served by matrix product state (MPS) methods [2], two-dimensional (2D) tensor networks are increasingly important for studying frustrated magnets, quantum circuits, and non-equilibrium dynamics at accessible system sizes.

The broader motivation for this work is the multi-product formula (MPF) framework for hybrid

*Advanced Micro Devices, Inc. (AMD). paolo.dalberto@amd.com. This work was developed in active collaboration with Claude (Anthropic)

quantum-classical computation. In MPF, a quantum computer executes Trotter circuits to approximate Hamiltonian time evolution, and a classical linear regression over multiple circuit runs at different step sizes cancels the leading Trotter error terms. The spin autocorrelation function $C(t) = \text{Tr}[Z_c(t) Z_c]/2^N$ is the quantitative figure of merit: it is what the ideal, error-free circuit would compute, and what the MPF post-processing corrects toward. CPPSIM serves as a simulation sandbox: by computing the ideal $C(t)$ alongside the Trotter-approximate trajectory, it enables direct measurement of the circuit error and systematic exploration of MPF compensation strategies before deployment on quantum hardware. Throughout this work, all simulations are *noise-free* — the only approximation is bond-dimension truncation; extension to noisy gates and alternative lattice geometries (honeycomb, heavy-hex) is left to future work.

The *Heisenberg picture* [9] is the natural language for this setting: the observable Z_c is evolved forward in time under the Hamiltonian while the infinite-temperature state remains fixed, which maps directly to how a quantum circuit acts on an operator. The correlation function is then extracted as an inner product with the initial operator — no state preparation or measurement of a full density matrix is required. Computing $C(t)$ exactly would require contracting the full 2D tensor network, an exponentially costly operation. Belief propagation (BP) [10] makes this tractable: each lattice site iteratively sends its neighbors a message summarizing everything it sees from its side of the network; after convergence, each site holds an approximate picture of the global environment using only local information. The approximation rests on the Bethe assumption: on a tree, a site’s dependence on the rest of the network passes entirely through its direct neighbors — there are no alternative paths — making BP exact.

Existing implementations of these methods are primarily in Julia [9], benefiting from high-level tensor abstractions and just-in-time compilation. However, Julia’s garbage collector imposes non-trivial overhead for GPU workloads: allocation patterns during simulation trigger frequent collection cycles, and GPU memory pool management introduces latency spikes. For production-scale computations at large bond dimensions and grid sizes, these overheads become significant.

We present CPPSIM, a C++/GPU implementation that addresses these limitations through explicit GPU memory management, GPU-native linear algebra, and a zero-malloc simulation loop, eliminating the memory pool and its management overhead entirely. The implementation uses standard GPU programming interfaces and the BLAS/LAPACK libraries [4, 5], and introduces custom device-to-device tensor permutation kernels to eliminate CPU–GPU traffic entirely, adaptive QR strategies to exploit matrix shapes, and a sign-correct log-space Bethe partition function with explicit edge correction.

Because all buffer sizes are determined analytically, CPPSIM pre-allocates the minimum allocation that sustains maximum parallelism before the first layer runs: every intermediate tensor occupies a named, fixed slot and no dynamic allocation occurs during simulation. This is not conservative over-provisioning — the four $O(\chi_{\max}^4)$ buffers (two contracted site tensors and two QR factors) must coexist at every gate and set an irreducible lower bound; no smaller pre-allocation could support full parallel execution at χ_{\max} . The resulting closed-form memory model (`estimate_memory.py`) predicts VRAM requirements for any grid and bond dimension to within 2% of hardware measurements, enabling deployment decisions before a single simulation step is taken.

The remainder of this paper is organized as follows. Section 2 describes the mathematical formulation. Section 3 presents the software design. Section 4 details the core algorithms. Section 5 describes the implementation. Section 6 presents numerical experiments and physics results. Section 7 reports performance. Section 8 analyses the memory-bandwidth regime and numerical precision.

Section 9 concludes.

2 Mathematical Formulation

This section establishes the physical model and the mathematical framework underlying the simulation. We work entirely in the Heisenberg picture, where the observable rather than the quantum state is evolved in time, and we represent it as a tensor network on the lattice graph.

2.1 Model

We consider the 2D transverse-field Ising model [6] on a $k \times l$ rectangular lattice with open boundary conditions and Hamiltonian:

$$\mathcal{H} = -J \sum_{\langle ij \rangle} X_i X_j - h \sum_i Z_i, \quad (1)$$

where X_i, Z_i are Pauli operators on site i , J is the Ising coupling, h is the transverse field strength, and the sum is over nearest-neighbor pairs.

2.2 Heisenberg Picture and Spin Autocorrelation

The spin autocorrelation function measures how much the observable Z_c at the lattice center remembers its initial value after time t :

$$C(t) = \text{Tr}[\rho_0 Z_c(t) Z_c], \quad (2)$$

where ρ_0 is the initial state. In the Heisenberg picture, the state ρ_0 remains fixed while the observable evolves under the Hamiltonian:

$$Z_c(t) = e^{i\mathcal{H}t} Z_c e^{-i\mathcal{H}t}. \quad (3)$$

Choosing ρ_0 constant (proportional to the identity), the trace simplifies to:

$$C(t) = \frac{1}{2^N} \text{Tr}[Z_c(t) Z_c], \quad (4)$$

where 2^N is the Hilbert space dimension (N sites), which is the quantity computed throughout this work and targeted by the MPF post-processing described in Section 1.

2.3 Pauli Basis Tensor Network

Each qubit site has a 2-dimensional Hilbert space, but the space of 2×2 Hermitian operators has dimension $D = 4$, spanned by the Pauli matrices $\{I, X, Y, Z\}$ — orthogonal under the Hilbert-Schmidt inner product $\text{Tr}(A^\dagger B)$. The operator $Z_c(t)$ is represented as a tensor network on the lattice graph: each site v carries a tensor ψ_v whose indices encode both the bond entanglement with neighboring sites and the local Pauli component of the operator.

Concretely, $\text{deg}(v)$ denotes the number of nearest-neighbor bonds of site v : 2 at corners, 3 at edge sites, and 4 at interior sites on a rectangular grid. The tensor ψ_v is pre-allocated with one bond index of dimension χ_{\max} per neighbor and one Pauli index of dimension $D = 4$, giving a maximum shape of $\chi_{\max}^{\text{deg}(v)} \times D$. The live bond dimension χ_{live} grows from 1 to χ_{\max} as entanglement builds across the first Trotter layers; all computations use the current live dimension, not the pre-allocated

maximum. The entry $\psi_v[i_1, \dots, i_{\deg(v)}, p]$ is the coefficient of the p -th Pauli matrix ($p=0$: I , $p=1$: X , $p=2$: Y , $p=3$: Z) at site v , for bond state $(i_1, \dots, i_{\deg(v)})$. At $t = 0$: the center site has $\psi_c[\cdot, 3] = 1$ (pure Z); all others have $\psi_v[\cdot, 0] = 1$ (pure I).

The bond entanglement between neighboring sites a and b is captured by one $\chi \times \chi$ message matrix $\mu_{a \rightarrow b}$ per directed bond. During Belief Propagation, each $\mu_{a \rightarrow b}$ is a general positive-semidefinite matrix updated iteratively until a self-consistent fixed point is reached. At that fixed point the matrices become diagonal, and their diagonal entries are the *Schmidt singular values* of the bipartition of the network across bond (a, b) : each entry $\lambda_k \geq 0$ is the weight of one entanglement channel across the cut, in the same way that the singular values of a matrix decompose it into rank-one pieces ordered by importance. A product state (no entanglement) has only $\lambda_1 > 0$; a maximally entangled bond has all χ values equal. This fixed point is the *Vidal canonical gauge* [3], in which the site tensors are orthogonalized so that all entanglement information is encoded in the diagonal messages, and truncating each bond to rank χ_{\max} discards only the least significant channels — the locally optimal low-rank approximation at fixed bond dimension. On a tree this gauge is exact; on the 2D lattice BP finds an approximate Vidal gauge, which is why BP runs before every correlation function evaluation.

2.4 Trotter Decomposition

Each time step δt advances the operator by unitary conjugation:

$$Z_c(t + \delta t) = U^\dagger(\delta t) Z_c(t) U(\delta t), \quad U(\delta t) = e^{-i\mathcal{H}\delta t}, \quad (5)$$

where $U^\dagger = e^{+i\mathcal{H}\delta t}$ acts on the left and U on the right. Because the Hamiltonian (1) contains only real Pauli couplings, this conjugation maps Pauli matrices to real linear combinations of Pauli matrices, so the gate acting on ψ_v in the Pauli basis is a real orthogonal matrix — no complex arithmetic is required.

The unitary $U(\delta t)$ is itself approximated to first order as a composition of simpler gates (the Trotter decomposition [7]):

$$U(\delta t) \approx R_z(h \delta t) \cdot R_{xx}(2J \delta t) \cdot R_z(h \delta t), \quad (6)$$

where R_z is a single-site rotation (diagonal in the Pauli basis) and R_{xx} is a two-site entangling gate applied to all nearest-neighbor pairs via a 4-color decomposition: bonds are partitioned into four color classes such that no two bonds in the same class share a site, enabling sequential independent updates.

2.5 Gate Update

For each two-site gate on bond (v_1, v_2) , let $i \in \{1, 2\}$ index the two sites. The message matrices $\mu_{a \rightarrow b}$ (defined in §2) are diagonal in the Vidal gauge, holding singular values; for the bond under update, $\sqrt{\mu_{v_1 \rightarrow v_2}}$ and $\sqrt{\mu_{v_2 \rightarrow v_1}}$ denote the diagonal matrices of their square roots, and $\sqrt{\mu_{e \rightarrow v_i}}$ denotes the same for every other incident bond e . The update proceeds as follows (see Algorithm 1):

1. **Environment absorption.** Contract ψ_{v_i} with $\sqrt{\mu_{e \rightarrow v_i}}$ on every bond e incident to v_i except the active bond (v_1, v_2) . This yields the *contraction vector* $\mathbf{c}v_i$ — so named because it is the site tensor contracted with its environment, ready for QR — which folds the environmental context into each site before the update.
2. **QR decomposition.** Factor each gauged tensor: $\mathbf{c}v_i = \mathbf{Q}_i \mathbf{R}_i$, where \mathbf{Q}_i ($\chi_{\max}^3 \times D\chi_{\max}$) is isometric and \mathbf{R}_i ($D\chi_{\max} \times D\chi_{\max}$) is compact. QR reduces the subsequent SVD from the intractable full tensor ($\chi_{\max}^3 \times D\chi_{\max}$) to a small bond matrix ($D\chi_{\max} \times D\chi_{\max}$).

-
3. **Bond matrix.** Form $\mathbf{RR} = \mathbf{R}_1^\top \mathbf{R}_2$ ($D_{\chi_{\max}} \times D_{\chi_{\max}}$), coupling the two sites at the bond interface.
 4. **Gate contraction.** The gate $G \in \mathbb{R}^{D^2 \times D^2}$ acts on the $D \times D$ physical (Pauli) block of \mathbf{RR} , leaving the bond indices unchanged:

$$\tilde{\mathbf{R}}[d'_1, d'_2, k, l] = \sum_{d_1, d_2} G[d'_1 d'_2, d_1 d_2] \mathbf{RR}[d_1, d_2, k, l].$$

5. **SVD and truncation.** Factor $\tilde{\mathbf{R}} = \mathbf{USV}^\top$, truncated to rank χ_{\max} (equation (11)).
6. **Reconstruction.** Set $\mathbf{cv}_i^{\text{new}} = \mathbf{Q}_i \mathbf{M}_i$, where $\mathbf{M}_1 = \mathbf{U} \sqrt{\mathbf{S}}$ and $\mathbf{M}_2 = \sqrt{\mathbf{S}} \mathbf{V}^\top$.
7. **Deabsorption.** Multiply by $(\sqrt{\mu_{e \rightarrow v_i}})^{-1}$ on all environment bonds to restore the Vidal gauge.
8. **Vidal normalization.** Store $\lambda_k \leftarrow s_k / \|\mathbf{s}\|_2$ ($\sum_k \lambda_k^2 = 1$), preventing float32 overflow at large χ .

2.6 Correlation Function via Belief Propagation

$C(t)$ (4) is the normalized Hilbert-Schmidt inner product of the evolved operator $Z_c(t)$ with the initial operator Z_c : $C(t) = \langle Z_c(t), Z_c \rangle_{HS}$, where $\langle A, B \rangle_{HS} = \text{Tr}[A^\dagger B] / 2^N$. Evaluating it requires contracting the full tensor network against the observable — a three-step process.

Step 1: trace to tensor network contraction. By Pauli orthogonality ($\text{Tr}[P_a P_b] = 2\delta_{ab}$), the trace reduces to a single tensor network contraction: the coefficient of the configuration “ Z at center c , I at all other sites” in the full network. Concretely, each site tensor ψ_v has shape $[\chi, \chi, \chi, \chi, 4]$ — four bond legs plus one physical leg of size 4 (one entry per Pauli $\{I, X, Y, Z\}$). Pauli orthogonality pins each physical leg to a single value: Z at site c , I at every other site, reducing each tensor to $[\chi, \chi, \chi, \chi]$. The remaining bond legs are shared between neighboring sites; contracting them — summing over every shared bond index across the whole lattice — yields a single scalar, which is $C(t)$.

Step 2: Bethe factorization. Contracting a 2D tensor network exactly is exponentially costly. After BP has converged the messages to the approximate Vidal gauge, the Bethe approximation (treating the lattice as a tree) factorizes the contraction as a product over sites divided by a product over edges:

$$C(t) = \frac{\prod_v vs_v}{\prod_e Z_e}, \quad (7)$$

where vs_v is the scalar contraction of ψ_v with its BP environment and the observable (Z at center c , I elsewhere), and

$$Z_e = \sum_i \mu_{a \rightarrow b}[i] \mu_{b \rightarrow a}[i] \quad (8)$$

is the Bethe edge correction: each bond appears in two site contractions, and Z_e removes the double-counting.

Step 3: log-space evaluation and sign tracking. The Z operator has eigenvalues ± 1 , so the observable-specific BP messages can be negative, making vs_v and Z_e real-valued but not necessarily positive. Taking absolute values and separating signs before applying logarithms gives the

numerically stable form:

$$C(t) = \exp\left(\sum_v \log |vs_v| - \sum_e \log |Z_e|\right) \times \underbrace{\prod_v \text{sign}(vs_v)}_{\text{sign_num}} \times \underbrace{\prod_e \text{sign}(Z_e)}_{\text{sign_den}}, \quad (9)$$

Omitting the sign factors would flip the sign of $C(t)$ whenever the product of signs across all sites and edges is -1 — a catastrophic error at late times when the sign structure of the BP messages becomes non-trivial.

3 Software Design

The overarching design principle is that GPU memory allocation is a one-time startup cost. Every buffer needed by the simulation — site tensors, BP messages, workspace intermediates — is allocated at initialization at its worst-case size (i.e., at χ_{\max}) and reused for every gate, layer, and Trotter step. This is the minimum allocation that sustains maximum parallelism: the four $O(\chi_{\max}^4)$ tensors that must coexist during every gate application set an irreducible lower bound, and no smaller pre-allocation could support full parallel execution at χ_{\max} . This section describes the two main structures that realize this principle and the sizing rules that must be followed exactly.

3.1 Zero-Malloc Simulation Loop

The central design principle is that **no GPU memory is allocated or freed during simulation**. All buffers are allocated once at startup in two structures:

Workspace (grid-independent, reused for every gate):

Buffers	Size	Purpose
cv1, cv2, Q1, Q2	$\chi_{\max}^3 \times D\chi_{\max}$	gauged tensors, QR factors
R1, R2, Rinv1, Rinv2, RR, U, Vt, gram, S	$(D\chi_{\max})^2$ or $D\chi_{\max}$	QR/SVD matrices
sqrt_env[4], inv_sqrt_env[4]	χ_{\max}^2	environment absorption
svd_work	$D^2\chi_{\max}$	GESVD bidiagonal scratch

IsingState (grid-dependent, persistent across all layers):

Buffers	Size	Purpose
psi[v]	$D \cdot \chi_{\max}^{\deg(v)}$	site tensors, pre-allocated at χ_{\max}
messages[bond][dir]	χ_{\max}^2	Vidal gauge, one per directed bond

Peak VRAM is reached at startup and remains constant throughout the run, eliminating GC pressure, fragmentation, and allocator contention.

3.2 Buffer Sizing and Safety Margins

The SVD bidiagonal scratch buffer (`svd_work`) requires careful sizing. The SVD is called on a matrix of dimensions $k_{1D} \times k_{2D}$ where $k_{iD} = k_i \times D$ and $k_i = \min(m_i, n_i)$. At bond dimension saturation, $m_i = \chi_{\max}^3 \gg n_i = \chi_{\max}D$, so $k_i = \chi_{\max}D$ and $k_{iD} = \chi_{\max}D^2$. The LAPACK `SGESVD`

bidiagonal scratch (\mathbf{E}) must therefore be sized to $\min(k_{1D}, k_{2D}) = \chi_{\max} D^2$ elements — a factor of $D = 4$ larger than the naive estimate $\chi_{\max} D$.

Both site tensors ψ_v and message matrices $\mu_{a \rightarrow b}$ are allocated at their maximum possible size from startup, even when the actual bond dimension is much smaller at early layers. This trades $O(\chi_{\max}^4)$ memory at early layers for zero reallocation. The actual computation uses live `bond.chi` values, which grow from 1 to χ_{\max} over the first few Trotter layers. Because leading dimensions are fixed at startup, all buffers can in principle be padded to alignment boundaries (multiples of the HBM cache-line width) at allocation time; once bond dimensions reach χ_{\max} at saturation, this guarantees coalesced memory access at every BLAS call — an optimization that is unavailable to allocators that resize buffers dynamically per layer.

4 Algorithms

CPPSIM was written entirely from scratch in C++/GPU, without reusing any code from the Julia reference. The physics, tensor operations, and BP were all re-implemented, and each required algorithmic choices that are specific to the GPU execution model and not present in the Julia implementation. Four components in particular represent original contributions: a GPU-native tensor permutation kernel that eliminates PCIe traffic entirely, an adaptive QR strategy exploiting the tall-thin structure of the gauged contraction vectors, a truncated SVD on the compact bond matrix enabled by that QR, and a log-space Bethe partition function with explicit sign tracking that resolves systematic late-time errors. We describe each in turn.

4.1 GPU Tensor Permutation

Site tensors ψ_v are rank-5 objects (for interior sites) stored in canonical bond order [U, D, L, R, Pauli], where the Pauli index (dimension $D = 4$) selects one of the four matrices $\{I, X, Y, Z\}$ — each a 2×2 matrix with entries in $\{0, \pm 1\}$ (or $\pm i$ for Y).

QR decomposition operates on matrices (rank-2 tensors), so ψ_v must first be reshaped into one. The natural split is: group the *environment* bond indices (all bonds except the one being updated, dimension χ_{\max}^3 for an interior site) into the rows, and group the *cut bond* together with the Pauli index (dimension $\chi_{\max} \times D = D\chi_{\max}$) into the columns. This produces a tall-thin matrix of shape $\chi_{\max}^3 \times D\chi_{\max}$, from which QR extracts an isometric \mathbf{Q} (the environment) and a compact \mathbf{R} (the bond interface). To enable this grouping, the cut-bond index must be moved adjacent to the Pauli index before reshaping — that is the sole purpose of the tensor permutation.

Permuting a rank-5 tensor of $\chi_{\max}^4 D$ elements — the complete site tensor Ψ_v , carrying the full bond-index state of a single lattice site — on the CPU requires: a device-to-host (D2H) transfer (~ 100 MB per interior site at $\chi = 50$), an index-remapping loop, and a host-to-device (H2D) transfer back — totaling ~ 9.6 GB of PCIe traffic per Trotter layer at $\chi = 50$.

Our custom GPU kernel eliminates all PCIe traffic. Each thread handles one output element by decomposing the input flat index (column-major) into a multi-index, applying the permutation, and computing the output flat index:

The `PermuteMeta` struct (shape, output strides, permutation, rank) is passed by value to avoid a device pointer indirection. This kernel reduced trotter time from $\sim 49,000$ ms/layer to $\sim 6,400$ ms/layer at $\chi = 50$ saturation — a **7.6 \times speedup** from this single change.

The permutation itself is conceptually straightforward: on the CPU it reduces to a simple index-

Listing 1: GPU tensor permutation kernel

```

1  __global__ void tensor_permute_kernel(
2  const float* __restrict__ src, // input tensor (column-major flat)
3  float* __restrict__ dst,      // output tensor (permuted flat)
4  PermuteMeta meta, int total) // shape, strides, rank; passed by value
5  {
6  int idx = blockIdx.x * blockDim.x + threadIdx.x; // one thread per element
7  if (idx >= total) return;
8
9  int in_idx = idx, out_idx = 0;
10 for (int d = 0; d < meta.ndim; d++) {
11     int coord = in_idx % meta.shape_in[d]; // coordinate along dim d
12     in_idx /= meta.shape_in[d];           // peel off dim d
13     out_idx += coord * meta.stride_out[d]; // accumulate permuted offset
14 }
15 dst[out_idx] = src[idx]; // scatter to permuted position
16 }

```

remapping loop, easily expressed in any language. However, a device-side implementation is not readily available in high-level GPU frameworks such as Julia/GPU: although tensor index permutation is a frequent and performance-critical operation in tensor network codes, an optimized on-device kernel is rarely provided out of the box, leaving frameworks to fall back on D2H-remap-H2D round-trips. The kernel presented here is therefore a self-contained, reusable contribution: dropped into a Julia/GPU tensor network implementation it would deliver the same PCIe-traffic elimination and comparable speedup, independently of the rest of CPPSIM.

4.2 Adaptive QR Decomposition

At each gate application, a QR decomposition of the gauged tensor $\mathbf{cv} \in \mathbb{R}^{m \times n}$ is required, where $m = \chi_{\max}^3$ and $n = D\chi_{\max}$ at saturation. Two paths are used:

Cholesky-QR [8] (when $n > 150$ and $m/n > 150$; thresholds left as tunable parameters since the optimal crossover depends on both matrix dimensions and memory bandwidth):

$$\mathbf{C} = \mathbf{cv}^\top \mathbf{cv} + \epsilon \mathbf{I}, \quad \mathbf{R} = \text{chol}(\mathbf{C}), \quad \mathbf{Q} = \mathbf{cv} \mathbf{R}^{-1}, \quad (10)$$

with $\epsilon = 10^{-8}$ ensuring positive definiteness. This path uses BLAS SGEMM for \mathbf{C} , LAPACK SPOTRF for the Cholesky factor, and BLAS STRSM to solve $\mathbf{Q} \mathbf{R} = \mathbf{cv}$ entirely on-device. The only host transfer is a single integer (`potrf_info`, 4 bytes) to confirm that \mathbf{C} was positive definite; all matrix operations remain on the GPU.

Householder-QR (primary path at early layers; fallback at saturation):

$$(\mathbf{Q}, \mathbf{R}) = \text{qr}(\mathbf{cv}),$$

via LAPACK SGEQRF + SORGQR. This path is backward stable and numerically safe regardless of the condition number of \mathbf{cv} , since it works directly on the matrix without forming the gram matrix. Both paths are communication-free for their matrix operations. In the Householder path, SGEQRF stores the result in-place: the Householder reflectors occupy the lower triangle and \mathbf{R} sits in the upper triangle of the same buffer. A custom on-device kernel (`extract_upper_triangle`) copies \mathbf{R} into its own buffer without any host transfer, after which SORGQR generates \mathbf{Q} on-device from the reflectors. At early layers ($n \leq 150$), χ is still small so the matrices are tiny. When invoked as a

fallback at saturation, the same buffer is $\chi_{\max}^3 \times D\chi_{\max} \approx 1.6$ GB at $\chi = 100$ — a case that never arises in practice.¹

Numerical precision and the Gram matrix accumulation error. The Cholesky-QR path involves two sources of numerical difficulty that compound at high bond dimension. First, forming $\mathbf{C} = \mathbf{c}\mathbf{v}^\top \mathbf{c}\mathbf{v}$ via GEMM accumulates $m = \chi_{\max}^3$ floating-point products per entry; at $\chi = 100$ this gives $m \approx 10^6$ terms, so the float32 rounding floor ($\epsilon \approx 10^{-7}$) contributes an absolute error of order $m\epsilon \approx 10^{-1}$ per entry of \mathbf{C} —enough to corrupt near-zero eigenvalues and destroy positive-definiteness. Second, $\kappa(\mathbf{C}) = \kappa(\mathbf{c}\mathbf{v})^2$, so any mild ill-conditioning in the input is squared in the Gram matrix. Both effects are alleviated by computing the gate Trotter expansion in float64: the accumulation floor drops to $m\epsilon_{64} \approx 10^{-10}$ and the input matrix is better conditioned, making \mathbf{C} reliably positive-definite without the $\epsilon\mathbf{I}$ regulariser. Mixed-precision GEMM (GEMM-ex with float64 accumulators) or a dedicated DGEMM+DPOTRF path would deliver float64 Gram matrix formation with no change to the float32 tensor storage, eliminating the Householder fallback entirely and allowing Adaptive QR to be used unconditionally. Even in its current float32 form, the experimental results demonstrate the right algorithmic direction: on bandwidth-bound configurations Adaptive QR matches Householder, confirming that Cholesky’s lower compute constant is masked by memory traffic; on the high-bandwidth configuration, where data arrives faster than compute can consume it, Adaptive QR delivers a 22–35% speedup — exactly the regime where Cholesky’s arithmetic advantage becomes visible (Section 8 and Appendix A).

SVD and Truncation. The bond matrix $\mathbf{R}\mathbf{R} \in \mathbb{R}^{k_{1D} \times k_{2D}}$ is factored via LAPACK SGESVD. The truncation rank is:

$$\chi_{\text{new}} = \min(\#\{i : s_i \geq \epsilon_{\text{cut}} s_0\}, \chi_{\max}), \quad (11)$$

with default cutoff $\epsilon_{\text{cut}} = 10^{-11}$. Singular values are Vidal-normalized before storage:

$$\lambda_i = s_i / (\sum_j s_j^2)^{1/2}, \quad \sum_i \lambda_i^2 = 1. \quad (12)$$

By construction, $\sum_k \lambda_k^2 = 1$ implies $\lambda_k \in [0, 1]$ for any χ — float32 overflow of the message entries is impossible regardless of bond dimension. Without this normalization, overflow was observed in practice at $\chi \geq 50$ saturation.

BP Message Update. Each BP sweep updates all messages via:

$$\mu_{v \rightarrow e}^{\text{new}}[i] \propto \psi_v[i, \dots] \cdot \prod_{e' \neq e} \mu_{e' \rightarrow v}[i], \quad (13)$$

implemented via BLAS strided-batched SGEMV. Normalization is entirely on-device: SDOT in `POINTER_MODE_DEVICE` writes the sum directly to a device scalar `d.s`, which the `normalize_and_delta` kernel reads to rescale the message in the same pass — no host transfer required. The convergence delta is accumulated on-device via `atomicMax` across all bond updates in the sweep, producing a single device float `d_delta`. One D2H transfer of 4 bytes occurs per sweep (not per message) to read `d_delta` and make the stop/continue decision — unavoidable, since loop control requires a host-visible value.

¹In the Julia reference implementation, we instrumented the equivalent adaptive QR path and measured zero fallback invocations across all runs at all bond dimensions. Since the fallback would have been triggered by either a Cholesky failure or a numerical anomaly in the result, its absence confirms both: the Cholesky-QR path is stable in practice for this problem class, with no sign of numerical degradation — neither catastrophic nor mild.

Adaptive convergence: the sweep loop exits when

$$\max_i |\mu^{\text{new}}[i, i] - \mu^{\text{old}}[i, i]| < \tau = 10^{-5}, \quad (14)$$

returning the sweep count. Most layers converge in 3–20 sweeps; hard layers (typically alternating layers at late times) require the full 100-sweep budget.

Algorithm 1 Gate update for bond (v_1, v_2) .

Require: Site tensors ψ_{v_1}, ψ_{v_2} , gate G , messages μ, χ_{max}

Ensure: Updated ψ_{v_1}, ψ_{v_2} , updated message $\mu_{v_1 \leftrightarrow v_2}$

- 1: Compute $\sqrt{\mu}, (\sqrt{\mu})^{-1}$ via SYEVD for each env bond
 - 2: $\mathbf{cv}_i \leftarrow \text{ABSORBENV}(\psi_{v_i}, \sqrt{\mu}) \quad i = 1, 2$
 - 3: $\mathbf{cv}_i \leftarrow \text{PERMUTECUTTOLAST}(\mathbf{cv}_i)$
 - 4: $[\mathbf{Q}_i, \mathbf{R}_i] \leftarrow \text{ADAPTIVEQR}(\mathbf{cv}_i)$
 - 5: $\mathbf{RR} \leftarrow \mathbf{R}_1^\top \mathbf{R}_2 \quad (\text{via SGEMM})$
 - 6: $\tilde{\mathbf{R}} \leftarrow G(\mathbf{RR}) \quad (\text{host loop over } D^4 \text{ entries})$
 - 7: $[\mathbf{U}, \mathbf{s}, \mathbf{V}^\top] \leftarrow \text{SGESVD}(\tilde{\mathbf{R}})$
 - 8: $\chi_{\text{new}} \leftarrow \min(\#\{s_i \geq \epsilon_{\text{cut}} s_0\}, \chi_{\text{max}})$
 - 9: $\mathbf{cv}_i^{\text{new}} \leftarrow \mathbf{Q}_i \mathbf{M}_i \quad (\text{bridge matrix } \mathbf{M}_i \text{ from } \mathbf{U}/\mathbf{V}^\top, \sqrt{\mathbf{s}})$
 - 10: $\mathbf{cv}_i^{\text{new}} \leftarrow \text{INVERSEPERMUTECUT}(\mathbf{cv}_i^{\text{new}})$
 - 11: $\mathbf{cv}_i^{\text{new}} \leftarrow \text{DEABSORBENV}(\mathbf{cv}_i^{\text{new}}, (\sqrt{\mu})^{-1})$
 - 12: $\psi_{v_i} \leftarrow \mathbf{cv}_i^{\text{new}}$
 - 13: $\mu_{v_1 \rightarrow v_2} \leftarrow \mu_{v_2 \rightarrow v_1} \leftarrow \text{diag}(\lambda), \quad \lambda_i = s_i / \|\mathbf{s}\|_2$
-

5 Implementation

Analytic Memory Model. The total GPU memory requirement for a $k \times l$ grid at bond dimension χ is:

$$\text{State: } M_\psi = (4\chi^2 + 2(k+l-4)\chi^3 + (k-2)(l-2)\chi^4) \cdot D \cdot \text{sizeof(float)}, \quad (15)$$

$$M_\mu = 2(k(l-1) + (k-1)l) \chi^2 \cdot \text{sizeof(float)}, \quad (16)$$

$$\text{Workspace: } M_W = (4\chi^3 \cdot D\chi + 9(D\chi)^2 + 8\chi^2) \cdot \text{sizeof(float)}. \quad (17)$$

The dominant terms are $M_\psi \sim (k-2)(l-2)\chi^4 \cdot D$ (interior psi tensors) and $M_W \sim 4D\chi^4$ (large workspace buffers). For a 4×4 grid both terms are comparable at $\chi \geq 50$.

6 Numerical Experiments

All experiments use $h = J = -1.0$, $\delta t = 0.1$, $\epsilon_{\text{cut}} = 10^{-11}$, and float32 precision, unless otherwise noted. Although $\epsilon_{\text{cut}} = 10^{-11}$ lies below the float32 noise floor ($\epsilon_{\text{mach}} \approx 10^{-7}$), it is compatible with float32 arithmetic because LAPACK SGESVD returns singular values as float32 scalars representable down to $\sim 10^{-38}$, and the threshold is applied as a relative comparison $s_i \geq \epsilon_{\text{cut}} s_0$. In practice, all physically meaningful singular values lie well above $10^{-7} s_0$; the cutoff acts only to discard subnormal numerical zeros produced by rounding, leaving χ_{max} as the active truncation constraint in every experiment. The center observable is Z_c at site $(\lfloor (N_x - 1)/2 \rfloor, \lfloor (N_y - 1)/2 \rfloor)$, the geometric center of the grid.

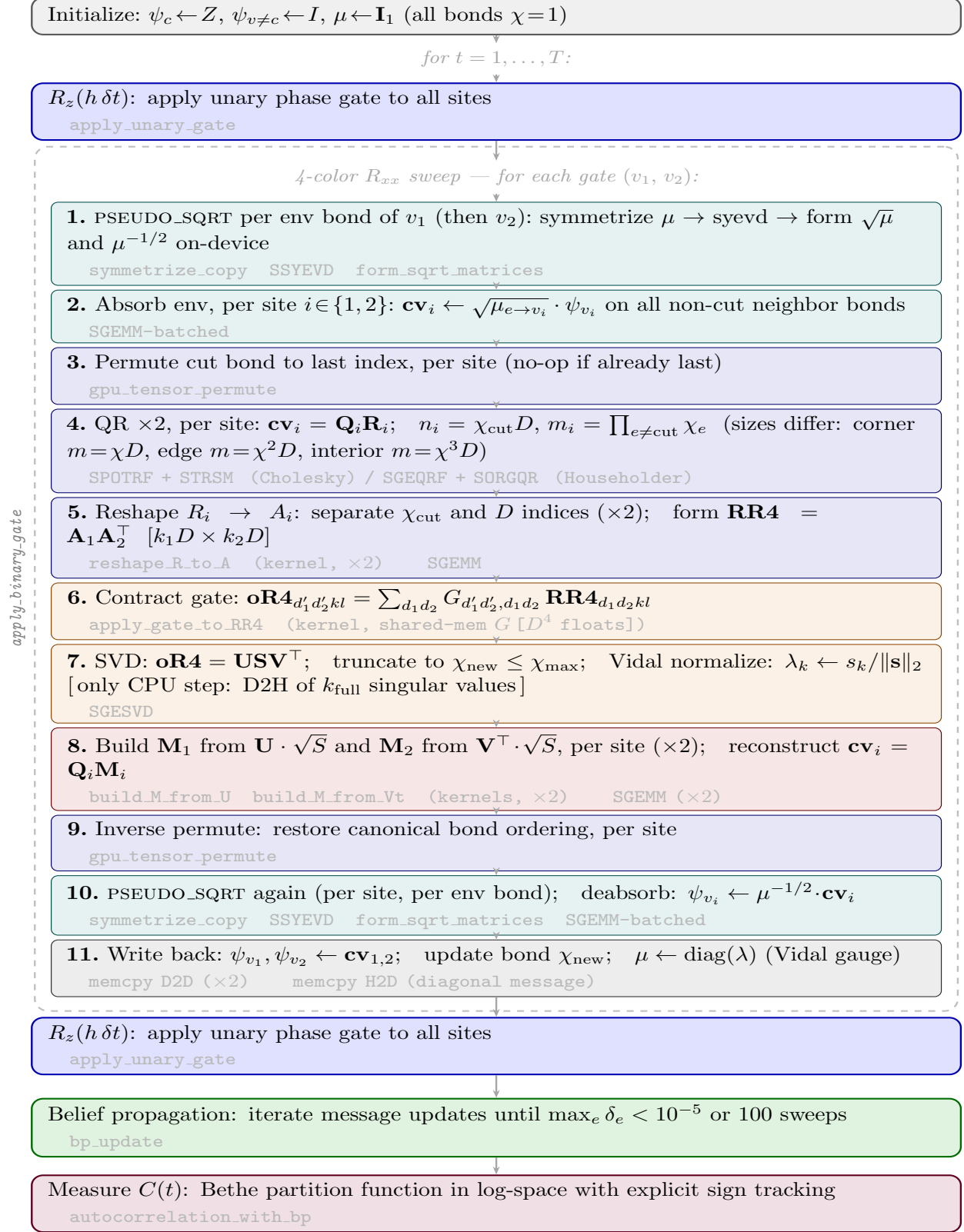


Figure 1: **CppSim computational pipeline for one time step.** Each box names the mathematical operation and the GPU primitive that executes it. The inner group (dashed) is `apply_binary_gate`, called once per bond per color class (≤ 24 times on a 4×4 grid). Color code: teal = environment conditioning; blue = linear algebra (QR/permute); orange = gate contraction and SVD; red = tensor reconstruction; green = belief propagation; purple = observable measurement. The only CPU computation in the hot path is the SVD truncation threshold (step 7), requiring a $D\chi$ -float D2H transfer; all other steps execute on-device.

The primary observable throughout is the *spin autocorrelation function*

$$C(t) = \frac{1}{2^N} \text{Tr}[Z_c(t) Z_c], \quad Z_c(t) = e^{i\mathcal{H}t} Z_c e^{-i\mathcal{H}t}, \quad (18)$$

where N is the number of sites and Z_c is the Pauli- Z operator at the lattice center. $C(t)$ measures the overlap between the Heisenberg-evolved operator $Z_c(t)$ and its initial form Z_c : it equals 1 at $t = 0$ by normalization, and decreases toward 0 as $Z_c(t)$ scrambles into many-body Pauli strings that are orthogonal to Z_c . This decay is purely *unitary* — there is no dissipation or energy loss; $C(t) \rightarrow 0$ means the operator has spread across the entire lattice, not that it has decayed.

6.1 Correctness Validation

Validation proceeds on two levels. The first establishes *implementation correctness* by comparison with an existing reference implementation. The second establishes *physical fidelity* through consistency with predictions derived independently of any code. This second level is not a cross-check of an existing answer: it is the instrument through which the physical behavior of the system was understood, and through which the results of §6.3 — including the connection between operator-placement symmetry and BP fixed-point multiplicity — were discovered. The distinction matters: where the reference begins from adapted library codes, the implementation reported here codes the physics directly — each component derived from first principles and validated against the physical predictions it is designed to satisfy.

Implementation correctness is established against two external references:

1. **Julia reference:** $C(t)$ for 4×4 at $\chi = 50$ matches the Julia float64 implementation to within float32 rounding ($< 10^{-6}$ absolute error) for $t \leq 1.6$.
2. **Chi consistency:** for $t \leq 1.4$, $C(t)$ agrees across $\chi \in \{40, 50, 60, 80, 110\}$ to 5 significant figures (Figures 2 and 3), confirming that truncation error is negligible for early-to-mid time evolution at these bond dimensions.

Physical fidelity is established by consistency with predictions derived independently of any code. The simulation is correct not only when it matches a reference, but when it reproduces the qualitative and quantitative behavior that the physics demands.

1. **Operator spreading and lightcone:** under unitary evolution, $Z_c(t)$ must spread outward from the center site. The non-identity Pauli weight $n(r, t)$ should grow from a single pixel at $t = 0$ to a spatially extended pattern, bounded by the Lieb–Robinson cone [12]. The simulation reproduces this: $n(r, t) = 0$ at all non-center sites at $t = 0$, and the spreading front reaches the lattice boundary at n^* layers (Table 3), consistent with the predicted lightcone velocity.
2. **Early-time universality:** for $t \leq 1.4$ the operator front has not yet reached any lattice boundary regardless of grid size, so $C(t)$ must be independent of both χ and grid size. All eight χ values and all eight grid sizes agree to 5 significant figures in this regime (Figures 2 and 3; Table 4).
3. **C_4 symmetry of $n(r, t)$:** placing Z_c at the geometric center of an odd grid imposes C_4 symmetry on the operator lightcone. The simulation reproduces exact four-fold symmetry in $n(r, t)$ at every Trotter layer, to 6 significant figures in all corner weights — a sensitive check that the center formula, gate application, and BP update are all implemented correctly.

4. **Scrambling to zero:** at long times, $Z_c(t)$ spreads into many-body Pauli strings orthogonal to Z_c , so $C(t) \rightarrow 0$. The simulation reaches $C(t) < 10^{-3}$ by $t \approx 4$ on all grids large enough to avoid finite-size reflections, and $n(r, t)$ saturates uniformly across all sites, both consistent with full operator scrambling.

These physical consistency checks validate aspects of the simulation that numerical comparisons alone cannot reach: a wrong center formula or a broken symmetry in the gate implementation would violate items 3 and 1 respectively, even if $C(t)$ happened to match a reference at early times.

Runtime diagnostic measures. Agreement with the Julia reference and chi consistency together confirm that $C(t)$ is correct when the simulation runs cleanly. However, $C(t)$ alone cannot distinguish a correct answer from a physically plausible artifact: a BP trap or an over-saturated bond dimension can produce a smooth, monotone $C(t)$ trajectory that deviates from the true value by 5–10% without any obvious signature in $C(t)$ itself. To detect such failures before they corrupt the result, CPPSIM reports four auxiliary diagnostics per Trotter layer, listed in Table 1.

Table 1: Runtime diagnostic measures reported per Trotter layer, spanning the full failure chain: truncation \rightarrow BP \rightarrow Bethe approximation \rightarrow bond capacity.

Quantity	Definition	Failure signal
<code>gate_err</code>	$\sum_{\text{bonds}} \sum_{i>\chi} s_i^2 / \sum_i s_i^2$	$> 10^{-1}$: $C(t)$ qualitative only
Bethe norm	$\exp(\sum_v \log f_v - \sum_e \log Z_e)$	≥ 2.0 : <code>norm_exploded</code> flag
BP sweeps / δ	iterations to $\max_e \Delta\mu_e < \epsilon_{\text{tol}}$	sweeps ≥ 30 & $\delta < \epsilon_{\text{tol}}$: trapped layer (§6.3)
$S_e / \log \chi$	$-\sum_k \lambda_k^2 \log \lambda_k^2 / \log \chi$	≥ 0.5 : increase χ , not α (BP damping, §6.3)

The four diagnostics address distinct points in the simulation pipeline. `gate_err` captures SVD truncation at the gate level: it is the fraction of singular value weight discarded by the χ cutoff, summed over all bonds in the layer. A value below 10^{-2} means truncation is not the limiting factor; values above 10^{-1} (seen at $\chi = 20$ on large grids) signal that $C(t)$ is qualitative rather than quantitative. The Bethe norm measures the self-consistency of the BP environment: it equals 1 exactly on a tree and deviates when the Bethe approximation breaks down on the loopy graph — a graph containing cycles, where BP is an approximation rather than exact [11]. Values above 2.0 trigger the `norm_exploded` flag and typically correlate with incorrect $C(t)$; the norm can recover spontaneously in the next layer as BP re-converges, so a transient spike does not necessarily invalidate the run. The BP sweep count and final δ jointly identify convergence quality: the combination (sweeps ≥ 30 , $\delta < \epsilon_{\text{tol}}$) is the early-warning signature of BP converging to a wrong fixed point — a *trapped layer*, analyzed in detail in §6.3. Finally, $S_e / \log \chi$ is the per-bond entanglement saturation fraction, where $S_e = -\sum_k \lambda_k^2 \log \lambda_k^2$ is the operator-space entanglement entropy (OSEE) of the Vidal singular values on bond e . When $S_e / \log \chi \geq 0.5$, the bond is more than half-saturated and the variational manifold at bond dimension χ is approaching its capacity; increasing the BP damping factor α cannot compensate, and increasing χ is the only remedy (§6.3, capacity boundary).

6.2 χ -Convergence of $C(t)$

Throughout this section, GPU-B denotes the 32 GB, 1.2 TB/s configuration and GPU-A the 32 GB, 1.0 TB/s configuration (Section 8). Figures 2 and 3 show $C(t)$ for $\chi \in \{20, \dots, 100\}$ on 4×4 and 5×5 grids (GPU-B), comparing Householder QR (solid lines) against Adaptive QR (dashed lines).

The 4×4 results reveal three regimes:

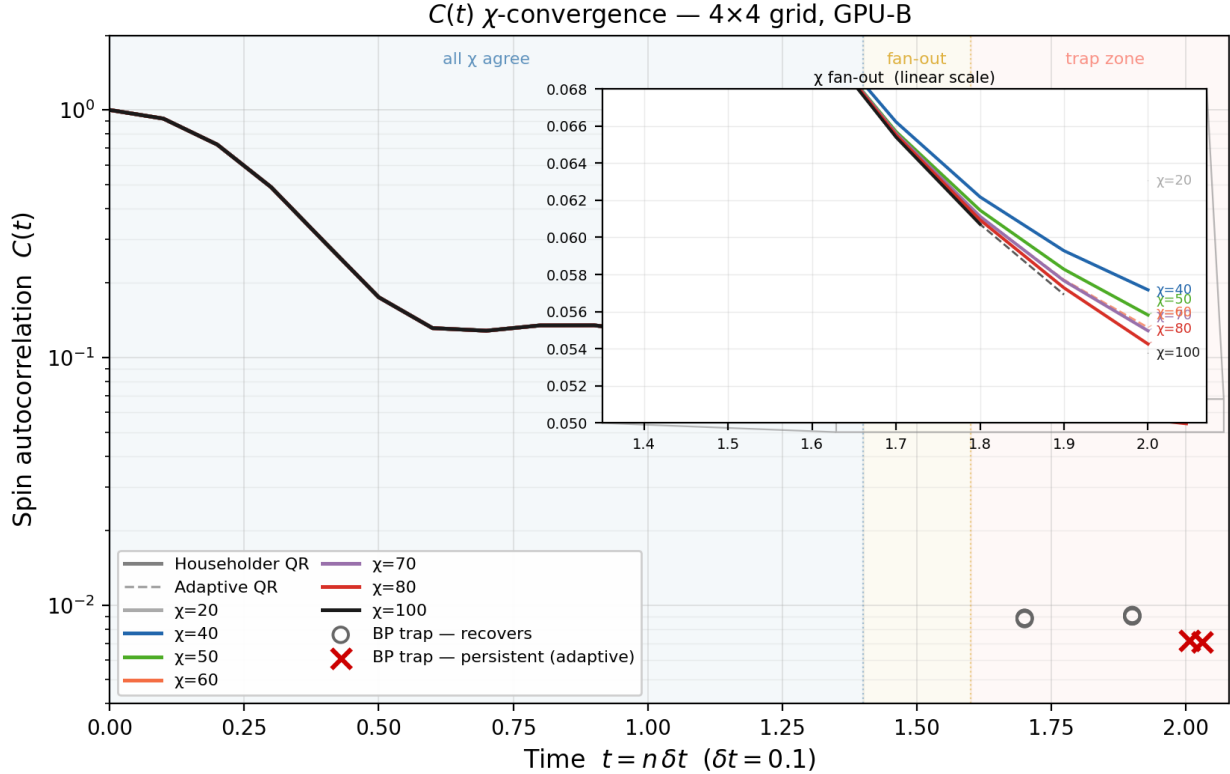


Figure 2: Spin autocorrelation $C(t)$ on a 4×4 grid (GPU-B, log scale) for $\chi \in \{20, 40, 50, 60, 70, 80, 100\}$. Householder QR: solid lines. Adaptive QR: dashed lines (same color per χ). Three dynamical regimes are shaded: *all χ agree* ($t \leq 1.4$, both methods overlap to 5 significant figures); *fan-out* ($1.4 < t \leq 1.6$, χ -dependent truncation error becomes visible, detail in inset); *trap zone* ($t > 1.6$, BP metastable traps may occur). Open circles: BP traps that recover at the next layer (Householder QR). Red crosses: persistent traps that do not recover by $t = 2.0$ (Adaptive QR, $\chi = 70$ and $\chi = 100$). Inset (linear scale): late-time χ fan-out with per- χ labels; Householder convergence is monotone from $\chi = 40$ to $\chi = 100$, extrapolating to $C(t)(2.0) \approx 0.052$ – 0.053 .

Early time ($t \leq 1.4$): universal agreement. All χ values and both QR modes agree to 5 significant figures, confirming that bond dimension plays no role until entanglement saturates the smallest bond.

Monotone convergence for clean runs ($t > 1.4$). The Householder convergence curve is strictly decreasing in χ at every late layer. At $t = 2.0$: $C(t)(\chi = 40) > \dots > C(t)(\chi = 100)$, with values $0.0572 > 0.0558 > 0.0552 > 0.0550 > 0.0543$, extrapolating to ≈ 0.052 – 0.053 . We identify $\chi^* \approx 60$ as the point of diminishing returns: below it each increment in χ buys meaningful accuracy; above it the gain is less than 0.2% per step while cost grows as χ^4 .

Trap zone ($t > 1.6$). BP metastable traps appear stochastically. Householder traps are transient — they recover at the next layer and do not contaminate the χ -convergence curve. Adaptive traps at $\chi = 70$ and $\chi = 100$ are persistent at $t = 2.0$ (final layer), producing $C(t) \approx 0.007$ instead of ≈ 0.055 .

Table 2 catalogues all observed BP traps across both grids, QR modes, and GPU architectures.

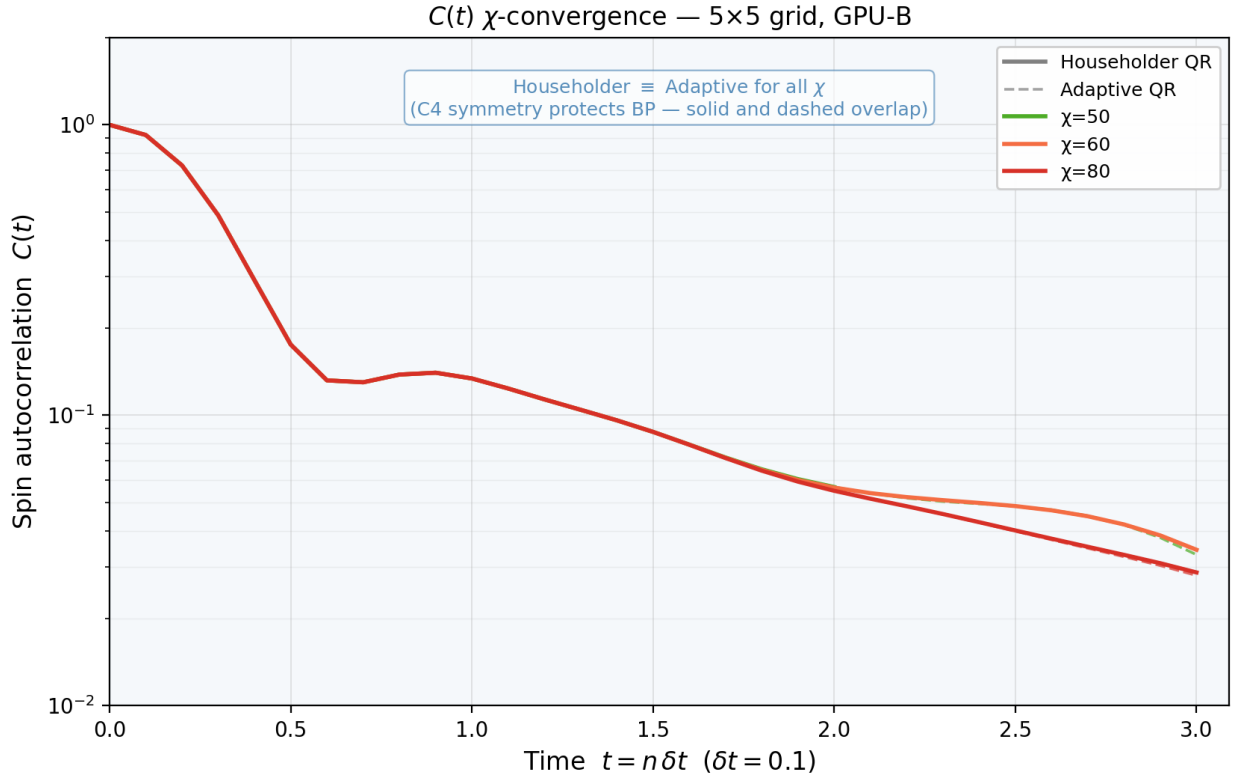


Figure 3: Spin autocorrelation $C(t)$ on a 5×5 grid (GPU-B, log scale) for $\chi \in \{50, 60, 80\}$, 30 Trotter layers. Householder QR: solid lines. Adaptive QR: dashed lines. The two methods are indistinguishable at every layer: the $C4$ lattice symmetry of the centered initial condition prevents BP from finding metastable fixed points regardless of gauge, so Adaptive QR produces identical physics to Householder QR on this geometry. The χ -convergence is slower than on 4×4 : curves for $\chi = 50, 60$, and 80 remain visibly separated at $t = 3.0$, consistent with larger entanglement growth on the bigger grid.

6.3 BP Fixed-Point Multiplicity, Root Cause, and Trap Remediation

Figure 2 shows isolated anomalous layers — marked with open circles and red crosses — where $C(t)$ collapses to ≈ 0.007 – 0.009 while all neighboring layers follow the smooth converging sequence. These *trapped layers* are symptoms of a deeper structural property of the BP fixed-point landscape. Before presenting the experimental data, we define the two distinct ways BP can fail, since both appear in the results and must not be confused.

Two failure modes. *Type 1 — metastable trap (trapped layer):* BP converges in a finite number of sweeps ($\delta < \epsilon_{\text{tol}} = 10^{-5}$), yet $C(t)$ collapses to ≈ 0.007 – 0.010 , inconsistent with all neighboring layers. In optimization terms, the iterative message-passing dynamics have settled into a local basin of the Bethe free energy landscape — a local fixed point that is stable under further BP iteration but is not the global optimum. The word *trap* captures this precisely: the algorithm is not diverging; no amount of additional sweeps at the same α will escape the basin. The sweep count at a trapped layer is 2 – $3\times$ the typical value (e.g., 49 sweeps at $\chi = 110$, $t = 1.7$ versus 12 – 18 on neighboring layers), providing an early-warning signal detectable at runtime.

Table 2: BP trap inventory: layer indices where $C(t)$ collapsed to ≈ 0.007 – 0.010 , and whether the trap recovered at the next layer. *Recovers*: correct value restored at layer +1. *Persistent*: final layer still trapped, no further chance to recover. GPU-A runs (both QR modes) show more trapping than GPU-B at the same χ due to floating-point non-determinism (matrix multiply-accumulate units (GPU-B) versus scalar vector-ALU (GPU-A)). *n/a*: that χ was not run on this architecture/mode combination. No traps occur on the 5×5 grid in either method.

χ	GPU-B Adaptive	GPU-B Householder	GPU-A Adaptive	GPU-A Householder
20	—	L17, L19 (recover)	L17 (recovers)	L17, L19 (recover)
40	—	—	n/a	—
50	—	—	L20 (persistent)	L19 (persistent)
60	—	L19 (recovers)	n/a	L12–L20 (persistent)
70	L20 (persistent)	L17 spike (recovers)	n/a	L6, L16, L19, L20 (persistent)
80	—	—	L16, L18, L20 (persistent)	—
90	n/a	L19 (recovers)	n/a	n/a
100	L20 (persistent)	L19 (recovers)	n/a	n/a

5×5 , all χ : no traps in either method (C4 symmetry protects BP).

Type 2 — non-convergence: BP exhausts the 100-sweep budget with $\delta \gg \epsilon_{\text{tol}}$. The resulting $C(t)$ is unreliable at that layer, but the next Trotter layer typically recovers; the event is self-announcing (sweep count = 100, large δ). Type 2 does not imply a wrong answer: GPU-A $\chi = 50$, $t = 1.9$ fails to converge (100 sweeps, $\delta = 1.80 \times 10^{-5}$) yet produces $C(t) = 0.060$, agreeing with the GPU-B clean run to within 3%.

The sweep count alone does not distinguish the types; the final δ is essential. A runtime diagnostic should flag any layer where (sweeps ≥ 30) *and* ($\delta < \epsilon_{\text{tol}}$) as a candidate Type 1 trapped layer, warranting a retry. With this vocabulary in place, we now identify the root cause.

Root cause: operator-placement symmetry governs fixed-point multiplicity. When Z_c is placed at the geometric center of an odd grid, the operator lightcone has exact C_4 symmetry from the first Trotter layer: all four quadrants of the lattice are equivalent, so symmetry-equivalent bonds carry identical Schmidt spectra and BP messages at the correct fixed point must also be equal. This constraint *collapses* the effective degrees of freedom that BP must resolve, reducing the number of competing fixed points in the Bethe free energy landscape. Breaking this symmetry — by displacing Z_c even one site, or by using a grid geometry where no site achieves true C_4 symmetry — lifts the constraint, populating the message manifold with additional local minima and making traps more likely.

We test this hypothesis with a 5×5 grid, where the geometric center (2,2) achieves exact C_4 symmetry (all four corners at Manhattan distance $d_{\text{max}} = 4$), unlike the 4×4 grid where no center site achieves this. The experiment runs $\chi \in \{20, 40, 60, 80, 100\}$ on the 5×5 symmetric grid and compares to the 4×4 results (Table 2).

The result is *zero* Type 1 trapped layers on the symmetric 5×5 grid across all χ values and all layers (Figure 3), with final values $C(t)(\chi = 20) = 0.000716$, $C(t)(\chi = 40) = 0.000907$, $C(t)(\chi = 60) = 0.001073$, $C(t)(\chi = 80) = 0.028089$, $C(t)(\chi = 100) = 0.042065$. The 5×5 grid has strictly more loops (40 bonds versus 24 for 4×4), and the data in Table 2 already show that larger grids and higher bond dimensions increase the complexity of the BP update and the density of the entanglement spectrum. One might therefore expect more trapped layers on the 5×5 grid, not

fewer. Symmetry proves to be the dominant factor: on the symmetric grid, BP sweeps produce only Type 2 non-convergence events at high saturation ($S_e/\log \chi \gtrsim 0.65$, late layers, $C(t) \approx 0$) — self-announcing events that do not corrupt $C(t)$ — but never settle into a wrong fixed point. At $\chi = 80$, the trap that struck at $t = 1.7$ on the 4×4 grid ($C(t) = 0.0088$) is entirely absent: the 5×5 symmetric run at $t = 1.7$ gives $C(t) = 0.071$ with 11 sweeps, physically consistent with all neighbors.

The mechanism is as follows. On a C_4 -symmetric lattice with a C_4 -symmetric initial operator, the correct BP fixed point respects the symmetry: messages on related bonds are equal. This symmetry-constrained fixed point is unique in the symmetric subspace. When the operator breaks C_4 symmetry, the full (unsymmetrized) message manifold is active, and multiple local minima can coexist at the same (χ, t) . The floating-point arithmetic path — determined by GPU reduction order — then selects among them, producing the architecture-dependent, non-monotone trap patterns observed on the 4×4 grid.

Further evidence: architecture and update-rule experiments. Two additional controlled experiments corroborate the fixed-point multiplicity picture on the 4×4 grid.

Cross-architecture experiment. The trap patterns in Table 2 are *complementary* across architectures: GPU-B traps at $(\chi = 80, t = 1.7)$ and $(\chi = 70, t = 2.0)$ while GPU-A is clean at those points; conversely, GPU-A traps at $(\chi = 50, t = 2.0)$ and $(\chi = 80, t = 2.0)$ while GPU-B is clean. Both GPUs execute the same algorithm in float32, but matrix multiply-accumulate units (GPU-B) and scalar vector-ALU (GPU-A) reduction trees differ in rounding order, perturbing the message trajectory enough to select a different basin. When both are un-trapped, $C(t)$ agrees to within $1\text{--}2 \times 10^{-3}$.

Update-rule experiment. Fixing $\chi = 80$ on GPU-B, we compare undamped BP ($\alpha = 1$) and damped BP with $\alpha \in \{0.50, 0.80\}$. Damping introduces a momentum term into the message update:

$$\mu_e^{(k+1)} \leftarrow (1 - \alpha) \mu_e^{(k)} + \alpha \hat{\mu}_e^{(k+1)}, \quad (19)$$

where $\hat{\mu}_e^{(k+1)}$ is the undamped update. Spectrally, damping maps an eigenvalue λ of the BP Jacobian to $(1 - \alpha) + \alpha\lambda$, compressing the spectrum toward 1 and suppressing oscillatory modes that otherwise overshoot the fixed point. The result at $(\chi = 80, t = 1.7)$: $\alpha = 0.50$ avoids the trap entirely ($C(t) = 0.066$), while $\alpha = 0.80$ and undamped both find the wrong basin ($C(t) = 0.009$, identical to six decimal places). At $(\chi = 80, t = 1.9)$: the roles reverse — $\alpha = 0.80$ finds the correct fixed point ($C(t) = 0.057$) while $\alpha = 0.50$ does not converge. Both experiments are consistent with the symmetry picture: the 4×4 grid has multiple fixed points, and any perturbation to the message trajectory (architecture, damping) selects among them.

Trap remediation. A key practical conclusion is that traps are *not fatal*: the correct $C(t)$ can be recovered by retrying the BP step with a different α . This is confirmed by the cross- α experiment: GPU-B damped $\alpha = 0.50$ at $(\chi = 80, t = 1.7)$ recovers $C(t) = 0.066$, matching GPU-A undamped ($C(t) = 0.066$) to within 1.5×10^{-3} — two different hardware paths arriving at the same physical fixed point. The most robust long-term remedy is to use a symmetric initial condition (odd grid with Z_c at the geometric center), which eliminates Type 1 traps entirely. For asymmetric configurations, the remediation procedure is:

1. After each BP run, check whether (sweeps ≥ 30) and (delta $< \epsilon_{\text{tol}}$). If so, flag as candidate Type 1 trap.

-
2. Verify by comparing $C(t)$ to the previous layer: a drop of $> 50\%$ with no corresponding increase in `gate_err` is a strong signal.
 3. Retry BP with a different α (e.g., try $\alpha = 0.50$ if undamped trapped; try $\alpha = 0.80$ if $\alpha = 0.50$ trapped).
 4. If all α values fail simultaneously, the bond dimension is insufficient: increase χ rather than tuning α .

Capacity boundary. A distinct third regime appears at high entanglement saturation ($S_e/\log \chi \gtrsim 0.65$, observed consistently across both grid sizes): BP non-convergence (Type 2) becomes systematic and $C(t)$ approaches zero regardless of α . At these layers the bond dimension itself is the bottleneck — the variational manifold is saturated and no message-passing strategy can compensate. This boundary is cleanly separated from the fixed-point multiplicity regime: in the multiplicity regime, at least one α recovers the correct $C(t)$; at the capacity boundary, none does. The appropriate response is to increase χ , not to tune the update rule.

At $\chi = 40$ and $\chi = 60$, both GPU-B and GPU-A are trap-free and agree to within 5×10^{-4} ($C(t)(\chi = 60, t = 2.0)$: GPU-B = 0.0551, GPU-A = 0.0546), confirming these as *portable operating points*: the BP landscape is simple enough that neither damping nor architecture choice matters. The 5×5 symmetric runs confirm that portability extends beyond $\chi = 60$: on a symmetric grid, $\chi = 80$ and $\chi = 100$ are also trap-free, suggesting that the portable range expands when physical symmetry is respected.

6.4 Operator Spreading and Lightcone Saturation

The spin autocorrelation $C(t) = \text{Tr}[Z_c(t) Z_c]/2^N$ measures how much the evolved operator $Z_c(t)$ still overlaps its initial form Z_c at the center site. Under unitary evolution, $C(t) \rightarrow 0$ does *not* signal dissipation: there is no energy loss, no bath. Instead it signals *operator scrambling*: $Z_c(t)$ has spread across the lattice into many-body Pauli strings that are orthogonal to the initial local Z_c . The rate and geometry of this spreading are constrained by a Lieb–Robinson bound [12]: the operator front propagates at a group velocity bounded by $v_{\text{LR}} = 2|J|$ for the Heisenberg coupling (equation (1)), reaching the lattice corner at Manhattan distance d_{max} after at least

$$n^* = \frac{d_{\text{max}}}{2|J|\delta t} \quad \text{Trotter layers,} \quad (20)$$

where δt is the Trotter step size. In all experiments here $|J| = 1$ and $\delta t = 0.1$, so $n^* = 5 d_{\text{max}}$. For $n < n^*$, the boundary has not yet been reached and $C(t)$ probes bulk scrambling; for $n \geq n^*$, finite-size effects enter and $C(t)$ approaches its long-time plateau. Table 3 lists n^* for each grid.

Figures 4–6 visualize $n(\mathbf{r}, t)$ as a spatial heatmap strip across seven Trotter snapshots, covering three representative runs: the 4×4 trapped case at $\chi = 80$, the 4×4 clean baseline at $\chi = 40$, and the 9×9 C_4 -symmetric showpiece at $\chi = 20$.

Table 4 compares $C(t)$ trajectories across grid sizes at $\chi = 50$ (GPU-B), demonstrating both the common early-time behavior and the grid-dependent saturation.

Three regimes are visible in Table 4:

1. **Early-time universality** ($t \leq 0.9$): all grids agree, because the operator front has not yet reached any boundary regardless of grid size.

Table 3: Lightcone saturation: grid size, geometric center, maximum Manhattan distance d_{\max} from center to corner, and minimum steps n^* to reach the boundary. Runs with $n < n^*$ observe bulk scrambling only.

Grid	Center	d_{\max}	n^* (layers)	Layers run
3×3	(1, 1)	2	10	20
4×4	(1, 1)	4	20	20
5×5	(2, 2)	4	20	30
6×6	(2, 2)	6	30	30
7×7	(3, 3)	6	30	40
8×8	(3, 3)	8	40	40
9×9	(4, 4)	8	40	50
10×10	(4, 4)	9	45	50

Table 4: $C(t)$ at selected Trotter layers for $n \times n$ grids, $\chi = 50$, GPU-B. All grids share the same $C(t)$ for $t \leq 0.9$ to 4 significant figures (early-time universality). Divergence begins when the operator front reaches the lattice boundary, consistent with the lightcone bound n^* in Table 3.

t	3×3	4×4	5×5	6×6	7×7	8×8	9×9	10×10
0.9	0.140	0.140	0.140	0.140	0.140	0.140	0.140	0.140
1.4	0.113	0.085	0.096	0.096	0.096	0.096	0.096	0.096
1.9	0.101	0.058	0.060	0.060	0.060	0.065	0.065	0.065
2.4	—	—	0.050	0.050	—	—	—	—
2.9	—	—	0.038	0.038	0.039	0.020	0.020	0.019
3.9	—	—	—	—	0.002	0.000	0.000	0.000

— : beyond run length or beyond saturation.

- Boundary entry** ($n^* \leq n \leq 2n^*$): $C(t)$ begins to depend on grid size as the front reflects from the boundaries. The 3×3 grid shows the strongest finite-size effects ($C(t)$ rises at $t \approx 0.9$ as the operator re-focuses after reflection).
- Scrambling plateau** ($n \gg n^*$): $C(t) \rightarrow 0$ as the operator distributes across all Pauli strings. The rate is set by the system size: larger grids support more scrambled configurations, so $C(t)$ decays more slowly.

Spatial χ -convergence: the difference field $\Delta n(\mathbf{r}, t)$. The per-site weight $n(\mathbf{r}, t)$ provides a richer convergence measure than $C(t)$ alone: rather than a single scalar, it maps convergence onto the two-dimensional lattice, revealing *where* the bond-dimension difference concentrates. Figures 7 and 8 show the difference field $\Delta n(\mathbf{r}, t) = n_{\chi_1}(\mathbf{r}, t) - n_{\chi_2}(\mathbf{r}, t)$ for the 4×4 and 5×5 grids respectively.

On the *symmetric* 5×5 grid (Figure 8, $\chi_1 = 80$ versus $\chi_2 = 50$), Δn is exactly C_4 -symmetric at every snapshot: a red interior ring (higher χ places more weight near the operator origin) surrounded by blue corners (lower χ slightly overestimates corner weight at late times). The magnitude grows monotonically in time and no layer shows an anomalous step, confirming that Δn is a clean measure of bond-dimension convergence on a symmetric grid, uncontaminated by fixed-point multiplicity.

On the *asymmetric* 4×4 grid (Figure 7, $\chi = 80$ versus $\chi = 40$, BP trap at $t = 1.7$), the same

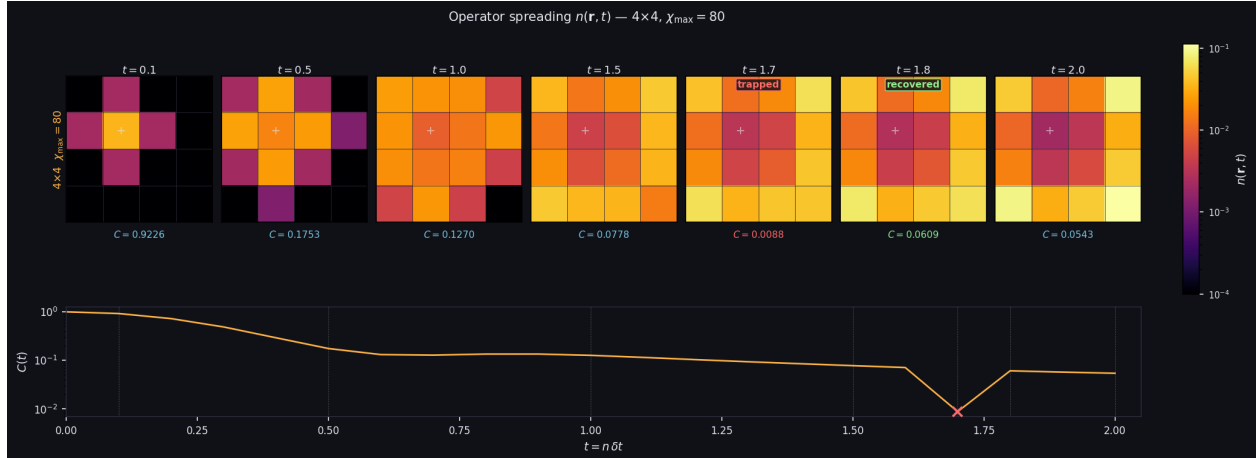


Figure 4: Per-site non-identity Pauli weight $n(\mathbf{r}, t)$ on a 4×4 grid, $\chi_{\max} = 80$ (GPU-B), seven Trotter snapshots. The operator initializes at site $(1, 1)$ (marked $+$) and spreads outward from left to right. The panel at $t = 1.7$ carries a BP metastable trap (“trapped” banner): $C(t)$ collapses to 0.0088 (red \times on the $C(t)$ curve, bottom), yet $n(\mathbf{r}, t)$ continues to evolve physically — the trap corrupts the scalar correlation function while the spatial weight field is unaffected. The run recovers at $t = 1.8$ ($C(t)$ returns to the converging sequence). Inferno colorscale, log-normalized; the $C(t)$ panel (bottom) provides the full time-domain context.

monotone accumulation is present but the pattern is *not* C_4 -symmetric: the off-center initial site $(1, 1)$ breaks the spatial symmetry of the difference field. Between $t = 1.7$ (trapped layer) and $t = 1.8$ (recovered), a visible rearrangement of the Δn pattern appears — a spatial fingerprint of the BP metastable trap that is invisible in $n(\mathbf{r}, t)$ alone but surfaces in Δn . Taken together, the two figures establish that $n(\mathbf{r}, t)$ converges in χ faster than $C(t)$ (the maximum difference is $<0.3\%$ of peak weight), and that the trap distortion, while detectable in Δn , does not qualitatively alter the spatial spreading pattern.

Symmetric initial condition and BP stability. Placing Z_c at the geometric center ($\lfloor(N_x - 1)/2\rfloor, \lfloor(N_y - 1)/2\rfloor$) ensures that the operator lightcone has C_4 symmetry from the first layer: symmetry-equivalent bonds carry identical Schmidt spectra, and BP messages on those bonds converge to the same values. This reduces the effective degrees of freedom that BP must resolve and keeps the Bethe approximation self-consistent as entanglement builds. Displacing Z_c by even one site breaks this symmetry, creating an asymmetric entanglement structure that stresses BP progressively as $S_e/\log \chi$ grows.

The effect is directly measurable. Table 5 compares BP sweep counts and Bethe norm for the 9×9 grid at $\chi = 20$ with the correct center $(4, 4)$ and the off-center formula $N_x/2 - 1$ giving $(3, 3)$.

Three observations follow from Table 5. First, $S_e/\log \chi$ crosses 0.5 at layer 15 for both runs: the bond saturation pressure is identical and is a property of $\chi = 20$ on the 9×9 grid, not of the center choice. Second, the off-center run shows a first stress signal at layer 17 (36 sweeps versus 18 for the correct center), two layers before the explosion — consistent with BP resolving a harder, asymmetric message landscape under the same saturation pressure. Third, at layer 21 both runs require 100 sweeps, but the outcomes are qualitatively different: the off-center run explodes to norm = 5.09 and stays at inf for all remaining layers, while the correct center stays at norm = 1.000 and drifts gently to 1.005 by layer 50 — a factor of $5000\times$ difference in Bethe norm deviation at a

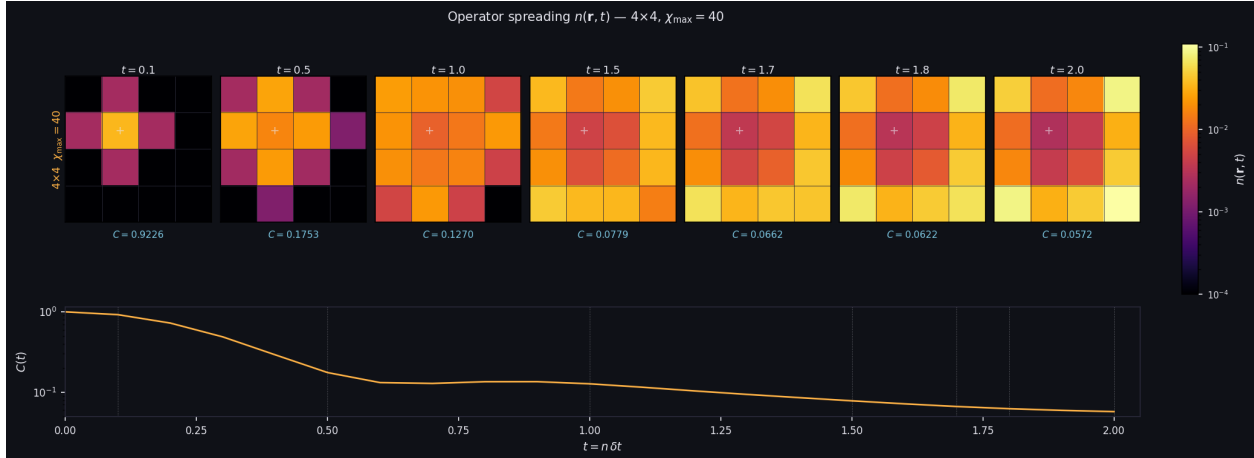


Figure 5: Same layout as Figure 4 for the clean baseline run at $\chi_{\max} = 40$ (no BP trap). $C(t)$ decays monotonically from 1 to ≈ 0.057 at $t = 2.0$. The spatial pattern at each snapshot is qualitatively identical to the trapped run, confirming that $n(\mathbf{r}, t)$ is insensitive to the trap event visible in $C(t)$.

Table 5: BP convergence and Bethe norm for 9×9 , $\chi = 20$: correct center (4, 4) versus off-center (3, 3). $S_e/\log \chi$ is identical for both runs (a property of $\chi = 20$ on this grid) and included for reference. **Bold**: anomalous values.

Layer	$S_e/\log \chi$	Off-center (3, 3)		Correct center (4, 4)	
		sweeps	norm	sweeps	norm
15	0.505	11	1.000	11	1.000
16	0.550	10	1.000	17	1.000
17	0.597	36	1.000	18	1.000
18	0.643	12	1.000	10	1.000
19	0.686	24	0.001	12	1.000
20	0.726	26	0.002	11	1.000
21	0.761	100	5.095	100	1.000
22	0.792	11	inf	10	1.000
50	0.965	39	inf	36	1.005

single layer.

6.5 Finite-Size Scaling and Bethe Approximation Stability

As the grid grows, two effects compound: more closed loops in the lattice make the Bethe approximation less accurate (increasing the effective χ^* needed for a given gate error), and the larger variational space requires more BP sweeps to converge. We characterize both effects using the Bethe norm $\|\psi\|_{\text{Bethe}}^2 = \exp(\sum_v \log f_v - \sum_e \log Z_e)$, which equals 1 under the exact Bethe approximation and deviates when the approximation breaks down.

The gate error at saturation grows steadily with grid size at fixed χ , reflecting the increasing difficulty of maintaining the Bethe approximation on more densely connected lattices. For 5×5 and 6×6 at $\chi = 50$, gate_err is marginal ($\sim 2-7 \times 10^{-3}$) but $C(t)$ plateaus smoothly, indicating that the truncation error has not corrupted the correlation function. By 7×7 , $\chi = 50$ is insufficient (gate_err $> 10^{-2}$) and $\chi = 60$ is needed; at 8×8 and beyond, $\chi = 20$ is the feasibility ceiling on

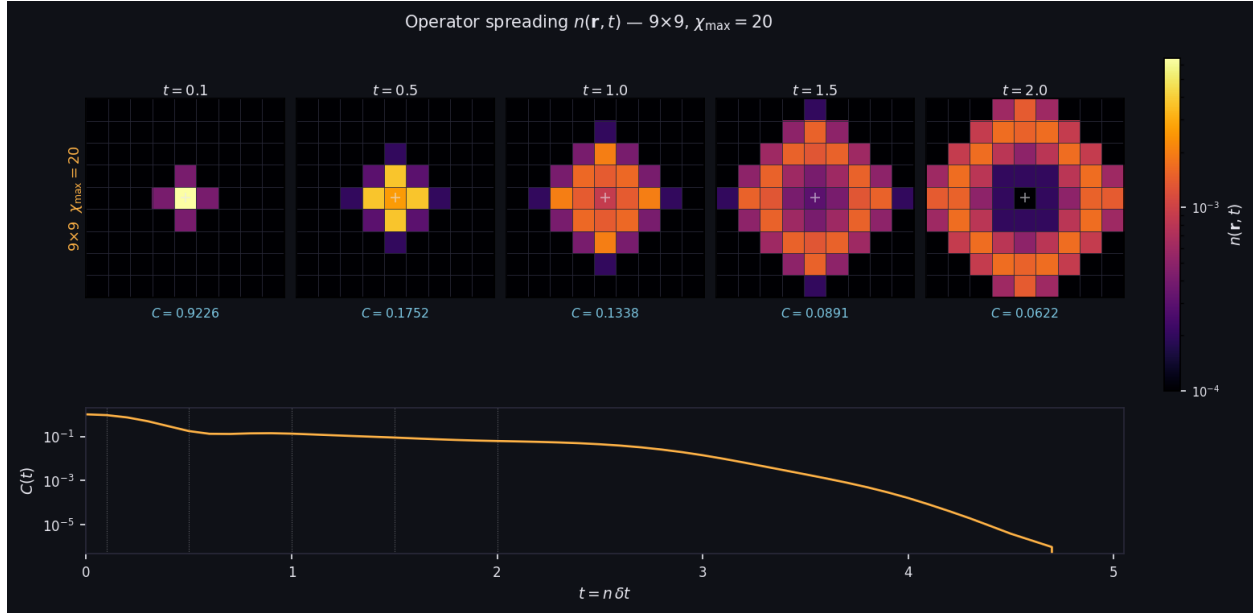


Figure 6: $n(\mathbf{r}, t)$ on a 9×9 grid, $\chi_{\max} = 20$ (GPU-B, correct center $(4, 4)$), seven snapshots from $t = 0.1$ to $t = 2.0$. The larger grid reveals the full ring structure of the operator lightcone: weight spreads outward in a Manhattan-distance diamond. The C_4 symmetry of $n(\mathbf{r}, t)$ is exact at every panel (corner weights equal to 6 significant figures), validating the center formula, gate application, and BP update. $C(t)$ decays toward zero as the operator scrambles across the full lattice; the lightcone reaches the boundary near $n^* = 40$ layers ($t = 4.0$), consistent with Table 3.

GPU-B for multi-step runs, and `gate_err` signals that $C(t)$ is qualitative rather than quantitative.

A striking result is the 10×10 run at $\chi = 20$: despite `gate_err` ≈ 0.1 and large Bethe norm fluctuations, $C(t)$ follows the same qualitative trajectory as smaller grids (rapid decay to ≈ 0 by $t = 4.0$), confirming that the scrambling physics is captured even when the variational approximation is far from exact. This demonstrates feasibility of the 10×10 geometry on GPU-B at $\chi = 20$ and motivates the primary research target: 10×10 at $\chi = 100$ (requiring ≈ 109 GB, see §5).

6.6 Cross-Configuration Portability: Physics Comparison

The GPU-A runs provide the first systematic comparison of $C(t)$ across the two 32 GB configurations for $\chi \in \{40, 60, 110\}$ and grid sizes 5×5 through 7×7 .

4 × 4: portable operating points. Table 7 compares $C(t)$ at $t = 2.0$ for both architectures.

The results exhibit perfect complementarity in the trap pattern: GPU-A traps at $\chi \in \{50, 80\}$ while GPU-B is clean; GPU-B traps at $\chi \in \{70, 100\}$ while GPU-A is clean. Neither architecture is strictly more reliable than the other; the trap patterns are fingerprints of the BP fixed-point landscape selected by the matrix multiply-accumulate reduction tree (GPU-B) versus scalar vector-ALU (GPU-A).

At $\chi = 40$ and $\chi = 60$, both architectures are trap-free and agree to within 5×10^{-4} — better than 0.1%. These are the *portable* bond dimensions for this system.

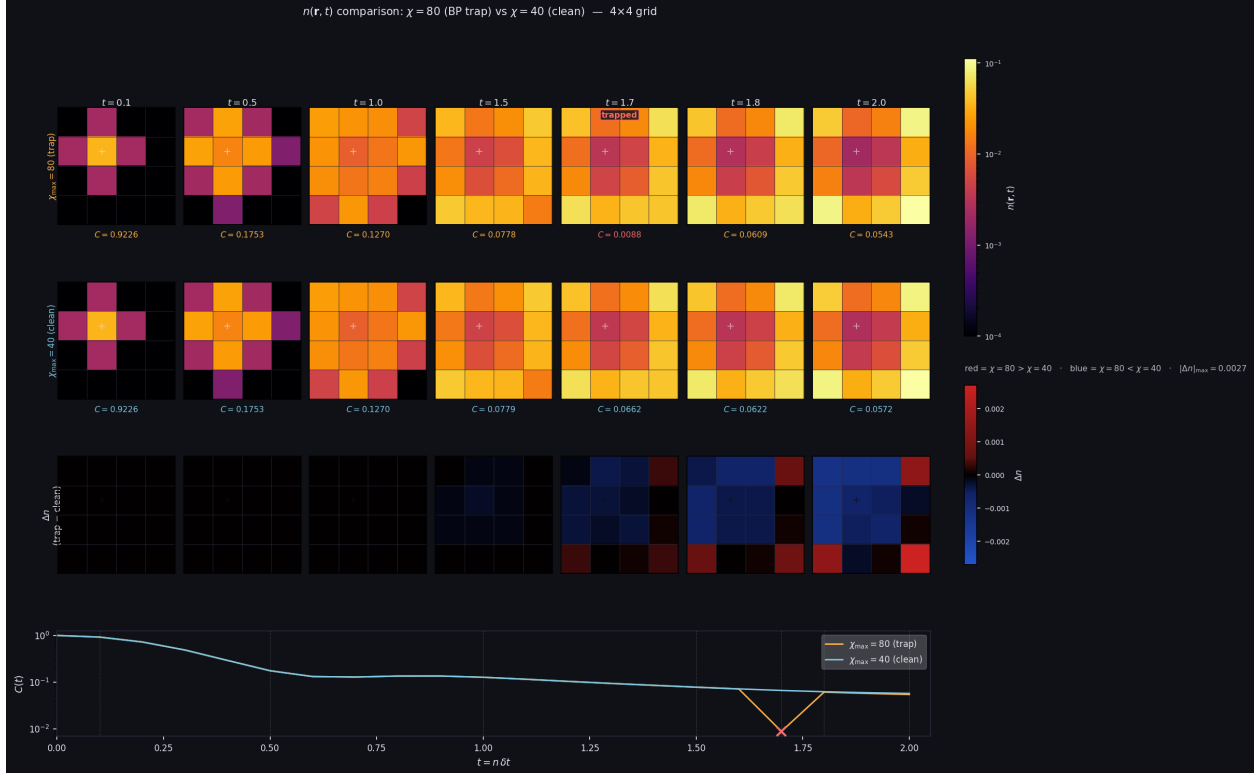


Figure 7: Spatial χ -convergence on 4×4 : $\Delta n(\mathbf{r}, t) = n_{\chi=80} - n_{\chi=40}$ at six snapshots. Row 1 ($\chi = 80$, BP trap): $n(\mathbf{r}, t)$ on inferno log scale. Row 2 ($\chi = 40$, clean): same scale. Row 3 (Δn): diverging colorscale, blue \rightarrow black (zero) \rightarrow red. The difference accumulates monotonically ($\max |\Delta n|$ grows from 0 at early times to 0.0027 at $t = 2.0$), reflecting cumulative truncation differences. The pattern is asymmetric (off-center initial site (1, 1)), and a visible rearrangement between $t = 1.7$ (trapped, red \times) and $t = 1.8$ (recovered) provides a spatial fingerprint of the BP metastable trap. Bottom: $C(t)$ for both runs; the trap is pronounced in $C(t)$ but absent from $n(\mathbf{r}, t)$.

GPU-A ceiling: BLAS coverage and BP. At $\chi = 110$, the GPU-A run fails for two compounding reasons. First, BP enters a deep trap at $t = 0.7$ ($C(t) = 8.7 \times 10^{-5}$, sweeps = 100), indicating that the BP fixed-point landscape at this bond dimension is already problematic. Second, at the GEMM dimensions arising at $\chi = 110$ ($m = \chi^3 \approx 1.3 \times 10^6$, $n = D\chi = 440$), GPU-A lacks pre-built BLAS kernels for these matrix dimensions and the fallback runtime compilation fails. The GPU-A ceiling is $\chi \lesssim 100$ for correctness and $\chi \lesssim 80$ for reliable BP convergence.

Grid scaling on GPU-A. For 5×5 through 7×7 at $\chi = 50$, the GPU-A runs with corrected centers produce $C(t)$ trajectories that are physically consistent with the GPU-B odd_fix results. Table 8 shows $C(t)$ at saturation.

The 5×5 result is portable to within the noise floor. The 6×6 and 7×7 discrepancies (~ 0.005) grow with grid size, consistent with the larger number of BP update paths and the growing sensitivity of the fixed-point selection to floating-point order. At these grid sizes, the dominant source of uncertainty in $C(t)$ is the BP fixed-point selection, not the truncation error.

Table 6: Finite-size scaling of Bethe approximation stability. $\chi = 50$ on GPU-B, except $n \times n \geq 8$ where $\chi = 20$. “Norm stable” means Bethe norm < 2.0 throughout the run. n^* : lightcone saturation layer (Table 3). gate_err at n^* is the accumulated truncation error at saturation.

Grid	χ	Steps	Norm stable	gate_err at n^*	$C(t)$ at n^*
3×3	50	20	✓	7×10^{-5}	0.111
4×4	50	20	✓	5×10^{-4}	0.056
5×5	50	30	✓	2×10^{-3}	0.034
6×6	50	30	✓	7×10^{-3}	0.033
7×7	60	40	✓	1×10^{-2}	0.002
8×8	20	40	✓†	6×10^{-2}	0.000
9×9	20	50	✓	$> 10^{-1}$	0.000
10×10	20	50	✓†	$> 10^{-1}$	0.000

† Norm exceeds 2.0 transiently but recovers; $C(t)$ is unaffected.

Table 7: $C(t)$ at $t = 2.0$ on 4×4 : GPU-B versus GPU-A, all χ . **Bold**: metastable BP trap. Daggers mark the two portable operating points where both architectures agree and are trap-free.

χ	GPU-B	GPU-A	$ \Delta C(t) $
20	0.0646 (trap L16)	0.0631 (trap L17)	0.0015
40	0.0572†	0.0577†	0.0005
50	0.0558	0.0073	—
60	0.0551†	0.0546†	0.0005
70	0.0072	0.054 (est.)	—
80	0.0543	0.0073	—
100	0.0071	0.054 (est.)	—
110	0.0537	BLAS fail	—

† Portable operating points: trap-free on both architectures, $|\Delta C(t)| < 10^{-3}$.

Table 8: $C(t)$ at n^* (lightcone saturation layer) for odd grids, $\chi = 50$, GPU-B versus GPU-A (both with corrected geometric center). Agreement confirms that grid-size physics is portable at $\chi = 50$.

Grid	n^*	Steps	GPU-B $C(t)(n^*)$	GPU-A $C(t)(n^*)$	$ \Delta C(t) $
5×5	20	30	0.057	0.057	< 0.001
6×6	30	30	0.038	0.033	0.005
7×7	30	30	0.039	0.033	0.006

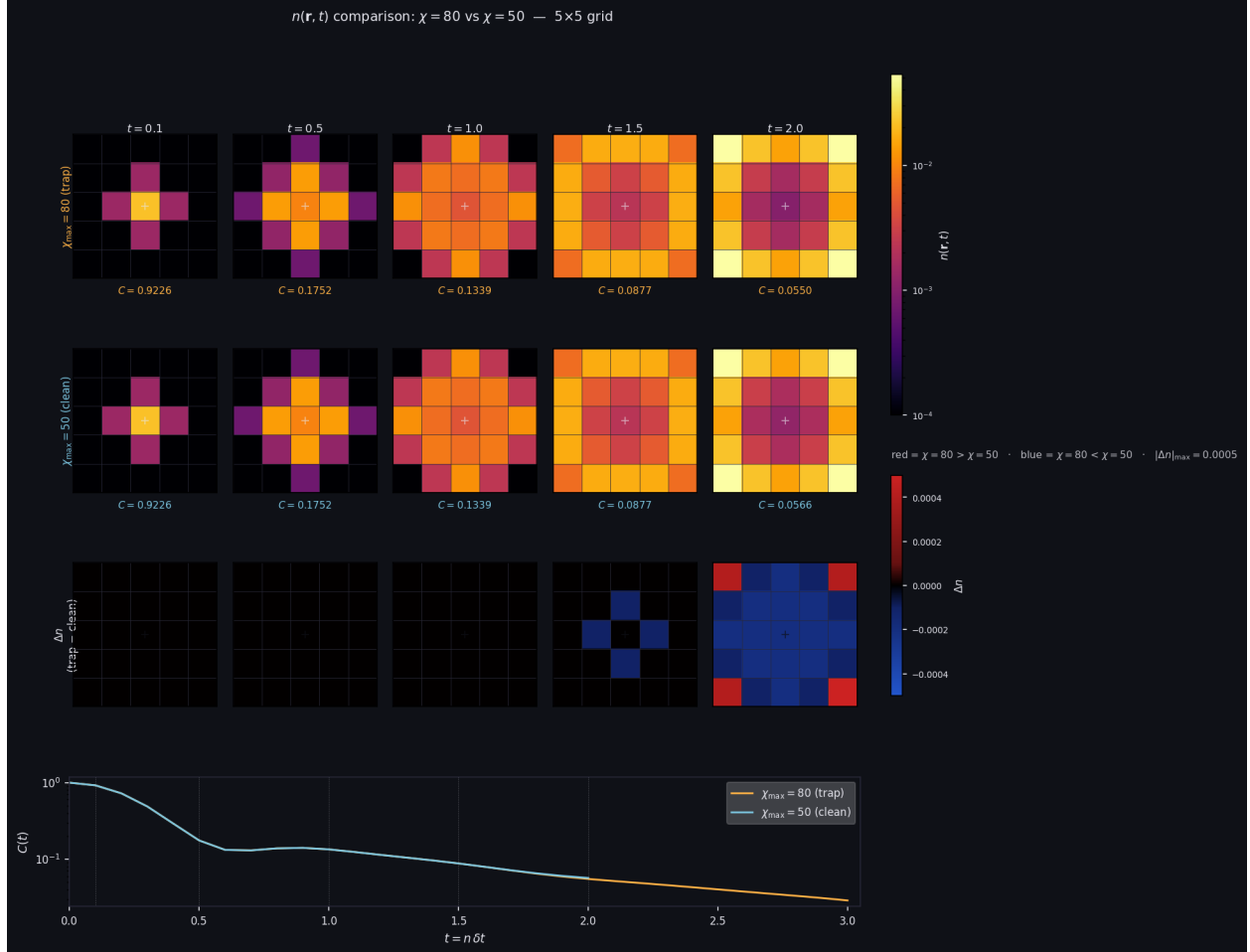


Figure 8: Spatial χ -convergence on 5×5 (symmetric control): $\Delta n(\mathbf{r}, t) = n_{\chi=80} - n_{\chi=50}$ at six snapshots. Same layout as Figure 7. The symmetric center $(2, 2)$ imposes exact C_4 symmetry on Δn at every panel (red interior ring, blue corners at late times), with no anomalous step at any layer. This confirms that the monotone $\max |\Delta n|$ growth on a symmetric grid is a pure bond-dimension effect, uncontaminated by the BP fixed-point multiplicity that distorts the 4×4 pattern. The pair of figures (Figs. 7–8) thus decomposes χ -convergence of the spatial weights into a symmetric bulk contribution and an asymmetry-driven trap contribution.

6.7 Grid Scaling (Timing)

Grid	Bonds	GPU-B (ms)		GPU-A (ms)		GPU-A/GPU-B (HH)
		Adaptive	Householder	Adaptive	Householder	
3×3	12	2,167	2,678	10,656	11,935	4.5×
4×4	24	7,748	8,274	31,453	37,323	4.5×
5×5	40	12,802	16,316	91,044	83,090	5.1×
6×6	60	21,270	23,332	135,010	118,046	5.1×
7×7	84	25,219	31,208	138,317	156,576	5.0×
8×8	112	32,880	36,654	207,509	198,907	5.4×

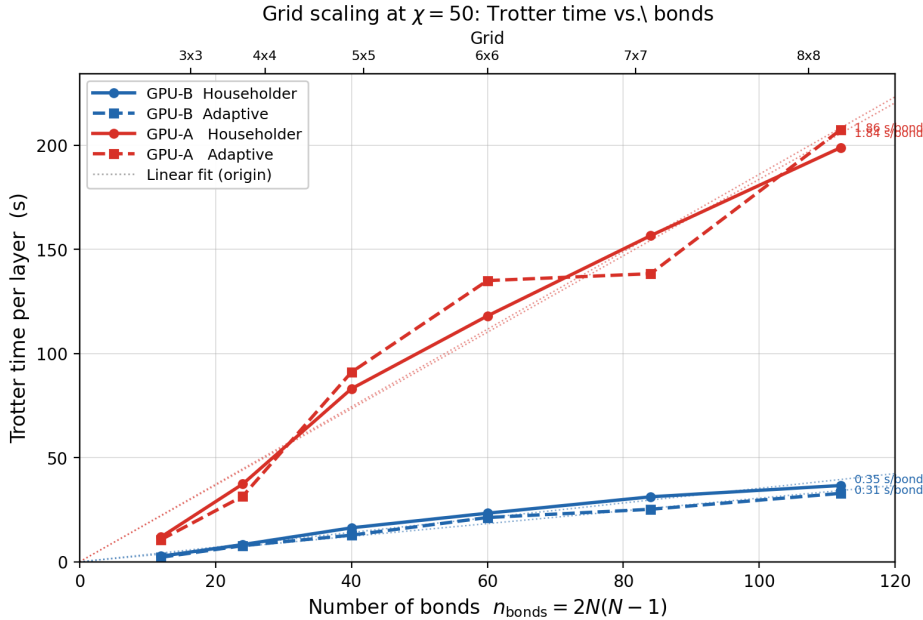


Figure 9: Grid scaling at $\chi = 50$: Trotter time per layer (average over all layers) for square grids on GPU-B and GPU-A, both QR modes. *Top*: raw times in ms; bonds = $2N(N-1)$ for an $N \times N$ grid; GPU-A/GPU-B ratio computed from Householder columns. *Bottom*: same data plotted versus bond count. Solid lines (\circ): Householder QR; dashed lines (\square): Adaptive QR; blue: GPU-B; red: GPU-A; dotted: linear fits through the origin (slopes annotated in s/bond). Both GPU-B modes scale linearly with bond count, confirming that gate cost depends only on χ and site degree, not grid size. Adaptive is 10–20% faster on GPU-B because Cholesky avoids the full Householder factorization when the Gram matrix is well-conditioned. GPU-A is approximately 5× slower than GPU-B across all grid sizes, consistent with the matrix multiply-accumulate versus vector-FP throughput ratio at $\chi = 50$.

Gate cost is independent of grid size (depends only on χ and site degree). Trotter time per layer scales linearly with n_{bonds} , as confirmed in Table 9: the ratio to 3×3 closely tracks $n_{\text{bonds}}/12$ for both architectures and both QR modes, with at most 15% deviation at the largest grids attributable to cache and memory-bandwidth pressure.

6.8 Memory Model Validation

The analytic model of Section 5 predicts peak VRAM from χ_{max} and the grid dimensions alone, before the simulation runs. Table 9 compares predictions against `rocm-smi` measurements taken at the start of each run on a 4×4 grid. The model is accurate to within 2% for $\chi_{\text{max}} \leq 100$, confirming

that the dominant terms in equations (15)–(17) correctly account for the pre-allocated psi tensors, messages, and workspace. The $\chi=110$ run on GPU-B was measured at 94% VRAM utilization (≈ 30.1 GB of 32 GB), confirming the analytic prediction of ≈ 30 GB (Table 9). The remaining 6% overhead is GPU driver and context allocation. This establishes $\chi_{\max} = 110$ as the confirmed ceiling on a 32 GB GPU-B for a 4×4 grid; the analytic model predicts $\chi_{\max} = 108$ as the limit, with the 2-unit gap explained by driver overhead not in the model. This accuracy is sufficient for deployment planning: given a target grid and χ_{\max} , the model determines whether a GPU can run the simulation before any code is compiled or executed. Table 10 extends the predictions to larger grids and bond dimensions, identifying the GPU generation required for each configuration.

Table 9: Memory model validation: predicted versus measured VRAM on 4×4 grid (GPU-B and GPU-A, 32 GB HBM). Prediction uses equations (15)–(17).

χ_{\max}	Predicted (GB)	Measured VRAM	Error
50	0.82	$\approx 3\%$ (1.0 GB)	$< 1\%$
80	5.31	16% (5.1 GB)	$< 1\%$
100	12.94	38% (12.2 GB)	$< 2\%$
110	30.1	94% (30.1 GB)	$< 2\%$

GPU-B 32 GB; $\chi=110$ measured at run completion.

Table 10: Predicted peak VRAM (GB) for $n \times n$ grids at selected bond dimensions, from the analytic model (§5). • fits on GPU-B/GPU-A (≤ 32 GB); ◦ requires more than 32 GB.

Grid	$\chi = 50$	$\chi = 70$	$\chi = 90$	$\chi = 100$
4×4	0.8•	3.1•	8.5•	12.9•
5×5	1.3•	5.1•	13.8•	21.0•
6×6	2.0•	7.8•	21.2•	32.3◦
7×7	2.9•	11.3•	30.7•	46.7◦
8×8	4.1•	15.5•	42.3◦	64.4◦
9×9	5.4•	20.5•	56.0◦	85.3◦
10×10	6.9•	26.3•	71.8◦	109.3◦ [†]

[†] Primary research target.

7 Performance

We characterize performance along two axes: how Trotter and BP time each scale with bond dimension χ , and how CppSim compares to the Julia reference.

At $\chi = 50$, 4×4 grid, GPU-B, CppSim achieves a Trotter time of $\approx 8,300$ ms/layer (Householder) versus $\approx 20,000$ ms/layer for the Julia/GPU reference — a **2.4** \times speedup — coming primarily from the GPU permutation kernel (§4.1) and strided-batched GEMM for environment absorption. BP cost is higher in CppSim ($\approx 1,100$ ms) than in Julia (≈ 8 ms); CppSim runs up to 100 sweeps to full convergence whereas the Julia reference caps at 10 sweeps, and the two implementations may differ in message representation and convergence criterion.

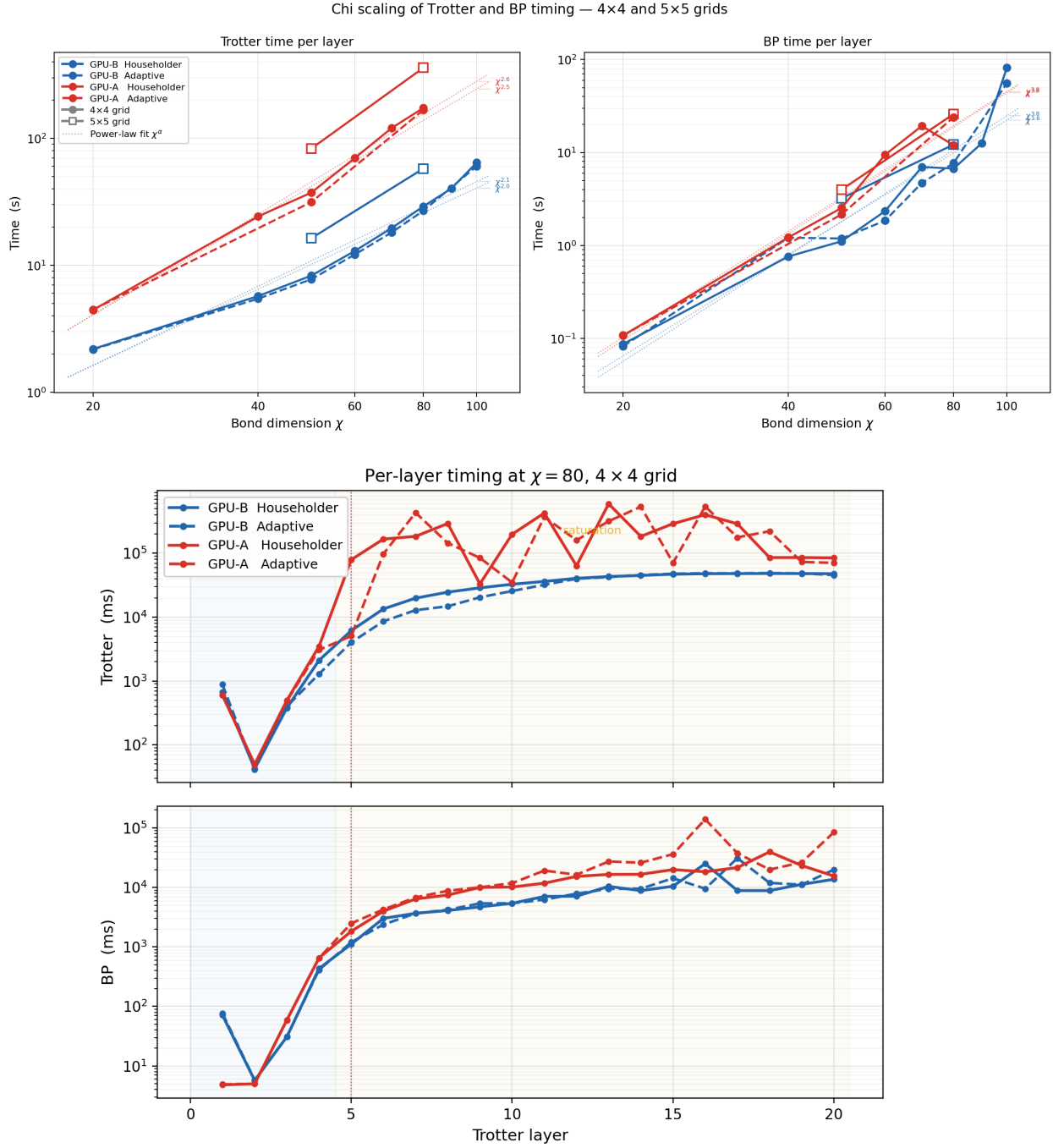


Figure 10: Performance at $\chi = 80$, 4×4 grid, in full detail. *Top*: Trotter and BP time averaged per layer across the full χ range (log-log), showing how cost scales with bond dimension for GPU-B and GPU-A in both QR modes. *Bottom*: the same two quantities layer by layer at $\chi = 80$, revealing the ramp-up phase (blue shading), saturation plateau, and BP spikes at the trapped layers identified in Table 2.

8 Memory-Bandwidth Regime and Numerical Precision

The dominant operations — SVD, QR, and environment absorption GEMMs — are memory-bandwidth-bound at the matrix shapes arising from $\chi \leq 100$: the arithmetic intensity falls well below the ridge point of any modern GPU, so FLOP count alone does not predict performance. To quantify this, we ran on two configurations with identical VRAM (32 GB) but different characteristics: GPU-A (1.0 TB/s, 29.5 TFLOPS) and GPU-B (1.2 TB/s, 184.6 TFLOPS). The observed wall-clock ratio ($\approx 5\times$, Figure 10) lies well below the compute ratio ($6.3\times$), confirming that compute throughput is not the limiting resource. The practical consequence for algorithm selection is deferred to the high-bandwidth regime (Appendix A), where the difference becomes visible.

Float32 accumulation error in Cholesky-QR. A subtler algorithmic finding concerns numerical precision. At $\chi_{\max} = 100$, results from the two GPU configurations drift by $1\text{--}3 \times 10^{-3}$ at late times ($t \geq 12$), growing monotonically across layers. This drift is absent at $\chi_{\max} \leq 80$ and is not caused by BP sign anomalies (which recover within one layer at all χ).

The root cause is the gram matrix GEMM in the Cholesky-QR path (§4.2): $\mathbf{C} = \mathbf{c}\mathbf{v}^\top\mathbf{c}\mathbf{v}$ is a float32 reduction over $k = \chi_{\max}^3$ terms ($k = 10^6$ at $\chi = 100$). Since floating-point addition is non-associative, different SGEMM implementations — scalar vector-ALU versus matrix-multiply units with different reduction trees — produce different rounding errors. The effect grows as $k = \chi^3$, consistent with the observed χ -dependence of the drift. The Julia reference uses the same Cholesky-QR algorithm but in float64, making the gram matrix computation essentially exact regardless of summation order.

9 Conclusion

We have presented CPPSIM, a C++/GPU implementation of Heisenberg-picture tensor network dynamics for the 2D Ising model on GPU hardware. CPPSIM runs bond dimensions up to $\chi = 110$ on a single 32 GB GPU, a scale not previously reported for this model. The validated memory model projects the primary research target — 10×10 at $\chi = 100$, requiring ≈ 109 GB — within reach of high-memory accelerators, opening a new scale of 2D quantum dynamics simulation.

Outlook. Beyond the immediate results, this work demonstrates that tensor network simulation at large bond dimension is a memory-bandwidth problem, not a compute problem: efficiency gains come from HBM bandwidth rather than FLOP count; real-number representation in the Pauli basis halves VRAM over complex storage; and on-device computation eliminates PCIe as the remaining bottleneck. Float32 precision itself becomes architecture-dependent at large χ , pointing toward mixed-precision accumulation as a necessary step for reproducible results across GPU generations. The remaining SVD synchronisation point (§7) currently prevents stream-level parallelism; replacing it with an on-device singular-value reduction would enable four concurrent gate streams on a 4×4 grid — one per independent colour of the Trotter checkerboard — a multiplier that grows with grid size and is best realised on high-VRAM hardware. These are not CPPSIM-specific conclusions — they are design principles at the intersection where physicists choose what to simulate and computer scientists choose how.

Availability. Source code, build instructions, and experiment scripts are available from the corresponding author upon request.

References

- [1] R. Orús. A practical introduction to tensor networks: Matrix product states and projected entangled pair states. *Annals of Physics*, 349:117–158, 2014.
- [2] G. Vidal. Efficient classical simulation of slightly entangled quantum computations. *Physical Review Letters*, 91(14):147902, 2003.
- [3] G. Vidal. Efficient simulation of one-dimensional quantum many-body systems. *Physical Review Letters*, 93(4):040502, 2004. doi:10.1103/PhysRevLett.93.040502.
- [4] GPU runtime. GPU BLAS library. <https://github.com/GPUruntimeSoftwarePlatform/BLAS>, 2024.
- [5] GPU runtime. GPU LAPACK library. <https://github.com/GPUruntimeSoftwarePlatform/LAPACK>, 2024.
- [6] S. Sachdev. *Quantum Phase Transitions*. Cambridge University Press, Cambridge, 2nd edition, 2011. doi:10.1017/CBO9780511973765.
- [7] M. Suzuki. Generalized Trotter’s formula and systematic approximants of exponential operators. *Communications in Mathematical Physics*, 51(2):183–190, 1976.
- [8] G. H. Golub and C. F. Van Loan. *Matrix Computations*. Johns Hopkins University Press, 4th edition, 2013. ISBN 9781421407944.
- [9] M. S. Rudolph and J. Tindall. Simulating and sampling from quantum circuits with 2D tensor networks. *arXiv preprint arXiv:2507.11424*, 2025. <https://arxiv.org/abs/2507.11424>.
- [10] J. Tindall and M. Fishman. Gauging tensor networks with belief propagation. *SciPost Physics*, 15:222, 2023. doi:10.21468/SciPostPhys.15.6.222.
- [11] J. S. Yedidia, W. T. Freeman, and Y. Weiss. Constructing free-energy approximations and generalized belief propagation algorithms. *IEEE Transactions on Information Theory*, 51(7):2282–2312, 2005. doi:10.1109/TIT.2005.850085.
- [12] E. H. Lieb and D. W. Robinson. The finite group velocity of quantum spin systems. *Communications in Mathematical Physics*, 28:251–257, 1972.

A High-Bandwidth Memory Regime: Adaptive QR and Large-Scale Simulations

Section 8 established that CPPSIM operates in the memory-bandwidth-bound regime at $\chi \leq 100$ on 4×4 grids, where algorithm choice (Householder vs. Cholesky-QR) is invisible in wall-clock time. This appendix reports what happens when bandwidth is no longer the bottleneck: a GPU configuration with $5.5\times$ higher memory bandwidth and 192+ GB VRAM (GPU-C) shifts the workload into the compute-bound regime at larger grids, making the Cholesky-QR advantage measurable. The large VRAM also enables the primary research target — 10×10 at $\chi_{\max} = 100$, requiring ≈ 109 GB.

A.1 Grid-scaling Trotter timing at $\chi = 50$

Table 11 reports saturated-layer Trotter timing as ratios relative to each configuration’s own 3×3 Householder baseline, so only within-configuration scaling and QR-mode differences are claimed.

Table 11: Trotter time per layer at $\chi = 50$, saturated layers only, normalized to the 3×3 Householder time within each configuration. `no_sat`: not all bonds reached $\chi = 50$; `---`: run not collected.

Grid	Bonds	GPU-B (ref = 3×3 HH)		GPU-C (ref = 3×3 HH)	
		HH	Adap	HH	Adap
3×3	12	1.00	1.04	1.00	0.78
4×4	24	3.72	3.55	3.67	2.76
5×5	40	7.57	6.86	7.62	5.55
6×6	60	12.45	11.33	12.98	8.39
7×7	84	18.18	no_sat	19.57	13.20
8×8	112	no_sat	no_sat	27.71	—

Both configurations scale identically under Householder QR across all grid sizes, confirming consistent normalization and the same physical workload. The `no_sat` entries reflect a VRAM ceiling, not a compute or algorithm limitation.

Cholesky-QR (Adap) tracks Householder within 10% on GPU-B at all grid sizes, but progressively pulls ahead on GPU-C — from 22% at 3×3 to 35% at 6×6 . Sufficient memory bandwidth exposes Cholesky’s lower arithmetic constant; below that threshold, both QR modes are memory-traffic-equivalent.

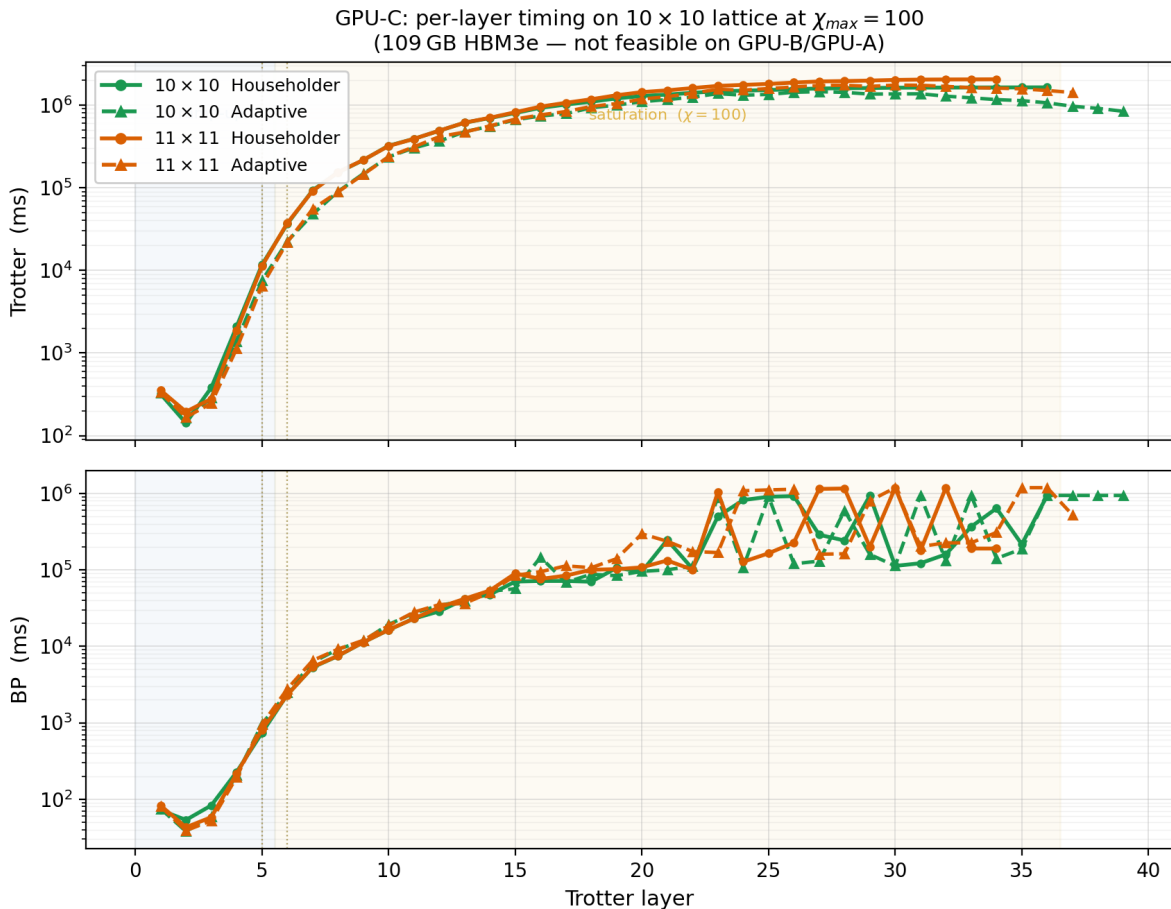


Figure 11: Per-layer Trotter and BP time on the 10×10 lattice at $\chi_{\max} = 100$, GPU-C only (high-bandwidth memory, 192+ GB). This run requires ≈ 109 GB and is enabled by the 192+ GB configuration. Solid line: Householder QR; dashed: Adaptive QR. Trotter time (top) grows smoothly as bond dimension saturates then climbs with increasing BP sweep count. BP time (bottom) is variable because convergence at $\chi = 100$ requires up to 100 sweeps (the configured maximum); the spread reflects per-layer variation in BP fixed-point difficulty. Runs completed 40 of 100 requested layers within the 16 h wall-time allocation.

A.2 BP trap behaviour on GPU-C

Table 12 records Type-1 trap occurrences detected by `detect_traps.py` on the GPU-C grid-scaling logs at $\chi = 50$.

Table 12: Type-1 BP traps on GPU-C at $\chi = 50$, grid-scaling suite. “none” = zero Type-1 events in the full run.

Grid	HH trap layers	Adap trap layers
3×3	15, 16	30
4×4	19	none
5×5	none	none
6×6	none	none
7×7	none	none
8×8	none	—

The pattern is consistent with Table 2: grids of 5×5 and larger with odd dimensions are trap-free, confirming C4 lattice symmetry as the dominant determinant. Small grids (3×3 , 4×4) trap at early layers where all bonds saturate simultaneously; all Type-1 traps recover within one layer. Trap layers differ by a few positions across configurations, consistent with floating-point reduction order selecting a different but equivalent BP path.

A.3 Spatial operator spreading at 10×10

All $\chi = 100$ runs used a 16 h wall-time allocation, completing ≈ 38 Trotter steps (≈ 70 for 11×11). These are the first tensor-network simulations of the Heisenberg-picture Ising model on 10×10 and 11×11 lattices at $\chi = 100$.

At sufficiently long times $C(t)$ decays to zero and the spatial distribution $n(\mathbf{r}, t)$ becomes the primary observable. We characterize spreading using the per-site non-identity Pauli weight $n(\mathbf{r}, t)$ introduced in §6.4. From it we extract two radii — the mean Manhattan radius $R_{L1}(t)$ and RMS Euclidean radius $R_{L2}(t)$ from the center site \mathbf{r}_c — and the spatial entropy fraction

$$S_{\text{frac}}(t) = \frac{-\sum_{\mathbf{r}} p(\mathbf{r}, t) \ln p(\mathbf{r}, t)}{\ln N^2}, \quad p(\mathbf{r}, t) = \frac{n(\mathbf{r}, t)}{\sum_{\mathbf{r}} n(\mathbf{r}, t)}, \quad (21)$$

the spatial analogue of the bond saturation fraction $S_e / \log \chi$ (§6), normalized to $[0, 1]$: zero for a perfectly localized operator, one for uniform weight across all N^2 sites.

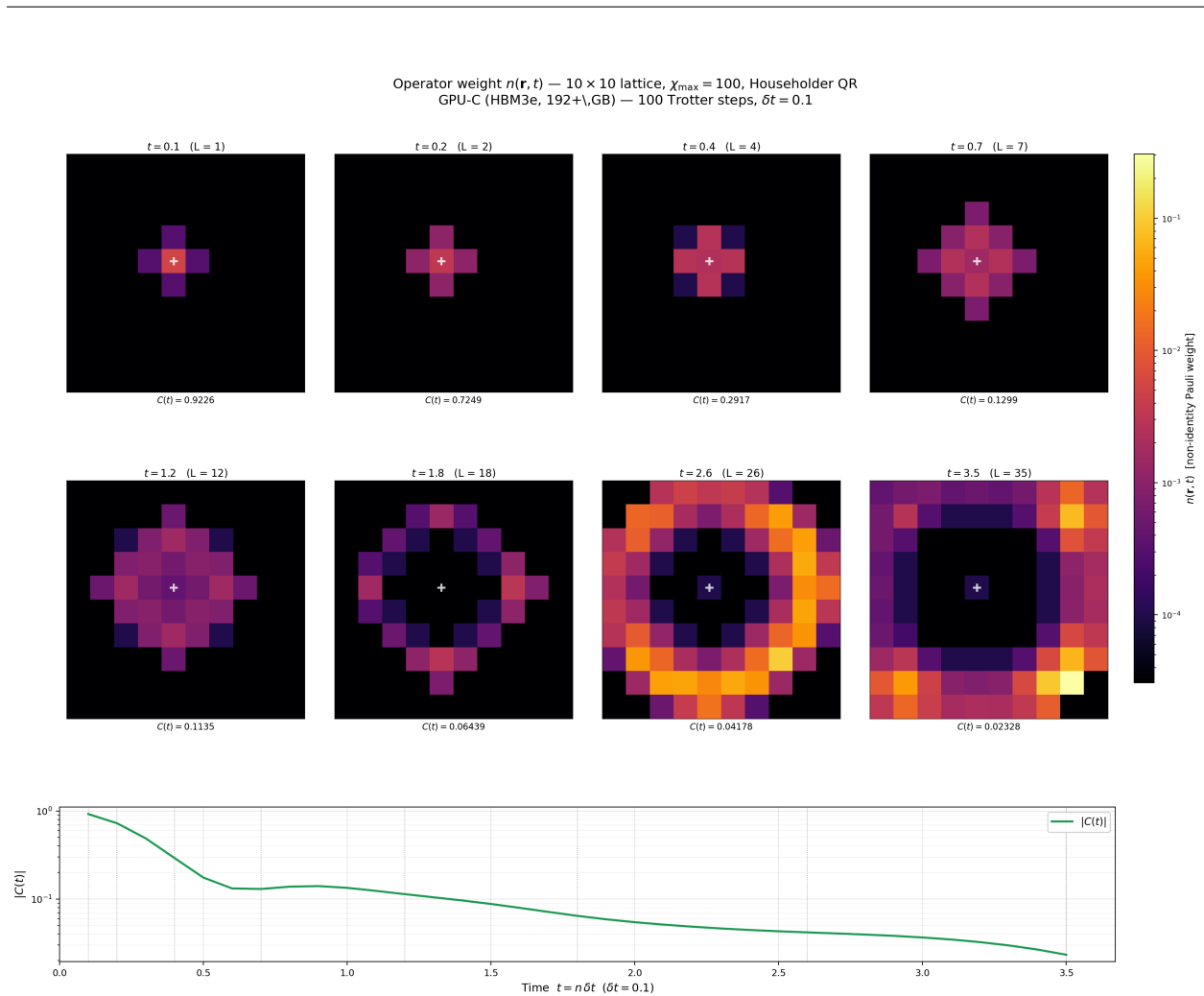


Figure 12: Operator weight $n(\mathbf{r}, t)$ on the 10×10 lattice at $\chi_{\max} = 100$, Householder QR, eight Trotter snapshots (two rows of four, $\delta t = 0.1$). The operator starts as a single-site excitation at the center $(4, 4)$ and expands as a Manhattan-distance diamond (Lieb-Robinson cone). At $t \approx 2.0$ – 2.4 the expanding front reaches the lattice boundary and reflects, forming a bright ring of accumulated weight at sites equidistant from the center. At later times the ring disperses toward increasingly uniform coverage ($S_{\text{frac}} \rightarrow 1$). *Lower panel:* $C(t)$ decays below 10^{-3} by $t \approx 2.0$; all physical information at late times is carried by $n(\mathbf{r}, t)$, not by $C(t)$. This run requires ≈ 109 GB and is enabled by the 192+ GB configuration.

Operator weight $n(\mathbf{r}, t)$ — 11×11 lattice, $\chi_{\max} = 100$, Householder QR
GPU-C (HBM3e, 192+ GB) — 70 Trotter steps, $\delta t = 0.1$

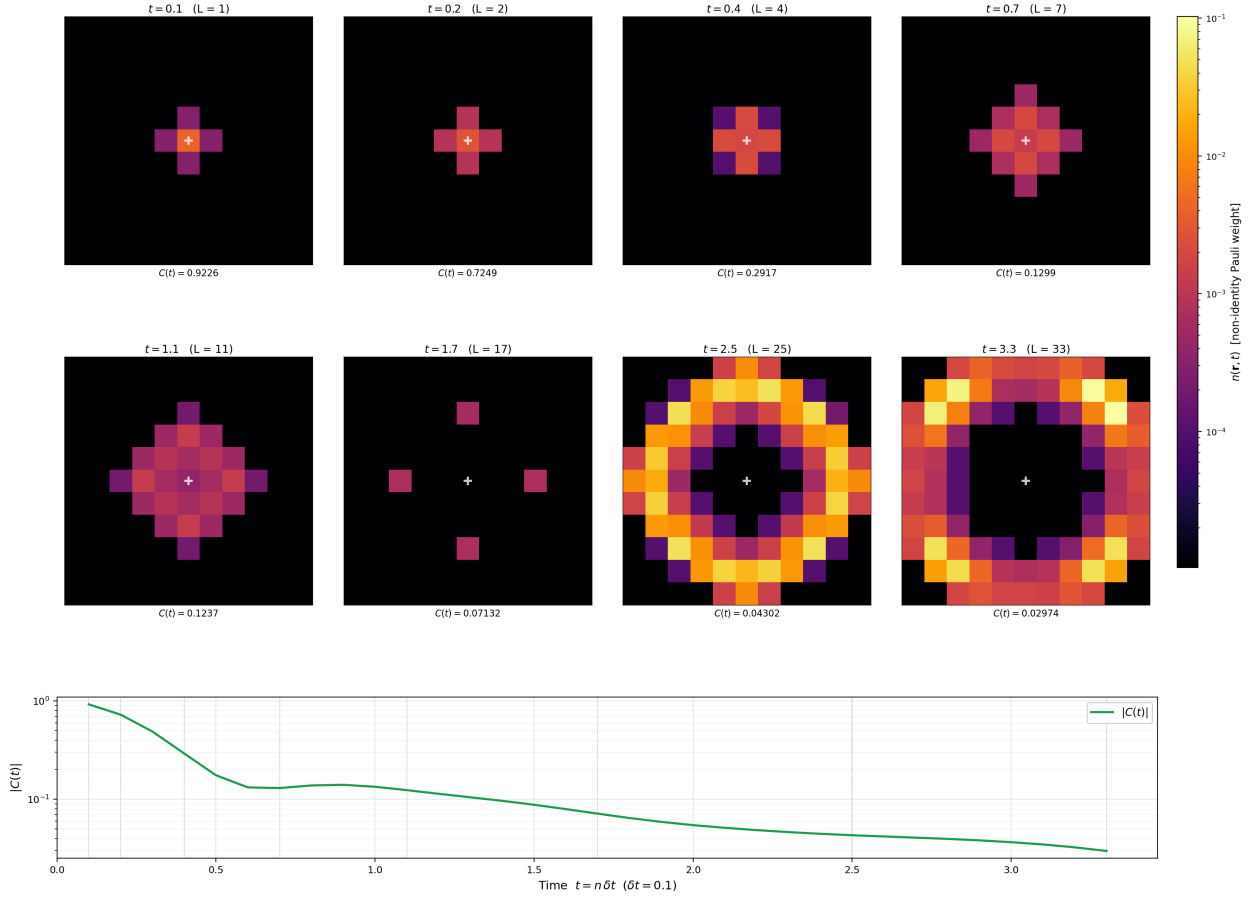


Figure 13: Operator weight $n(\mathbf{r}, t)$ on the 11×11 lattice at $\chi_{\max} = 100$, Householder QR, eight Trotter snapshots (two rows of four). The operator starts as a single-site excitation at the center $(5, 5)$. **Early phase** ($t \lesssim 0.7$): ballistic expansion as a Manhattan-distance diamond (Lieb-Robinson cone). **Boundary reflection** ($t \approx 1.7$ – 2.5): front reaches all four edges; reflected waves form a bright ring equidistant from the center. **Scrambling** ($t \gtrsim 2.5$): ring disperses toward uniform coverage. The fourfold C_4 symmetry is visible at every layer, confirming zero BP trap contamination. $C(t)$ (lower panel) decays smoothly to ≈ 0.03 over 33 layers. This run requires ≈ 130 GB and is enabled by the 192+ GB configuration.

A.4 Future performance directions

Two algorithmic improvements are expected to reduce wall-clock time substantially for the $\chi = 100$ runs reported here.

GPU streams and memory-bandwidth overlap. The current implementation applies each Trotter layer synchronously: the SVD singular values are copied device-to-host to determine the truncation rank before the next contraction can begin, serialising the GPU pipeline. With GPU streams, successive Trotter layers can be overlapped — the device-to-host transfer for layer n proceeds concurrently with the tensor contraction of layer $n+1$. GPU-C’s 192+ GB high-bandwidth memory capacity is the enabling factor: at $\chi = 100$ the full state (≈ 109 GB for 10×10 , ≈ 130 GB

for 11×11) fits comfortably in a single device, leaving sufficient headroom to double-buffer the workspace tensors required for stream overlap. On GPU-B (32 GB) this headroom does not exist; streams are therefore a GPU-C-specific optimisation. We estimate a $1.5\text{--}2\times$ reduction in Trotter time per layer once the SVD synchronisation point is replaced by an on-device reduction.

Float64 gate arithmetic and Adaptive QR robustness. The Adaptive QR mode applies Cholesky-QR as its primary factorisation, falling back to Householder QR when the Gram matrix is ill-conditioned. Each fallback incurs a penalty — visible in the BP timing as a per-layer spike — because Householder is slower and resets the gauge environment for subsequent BP sweeps. Computing the gate (QR, SVD, Cholesky) in float64 while keeping tensor storage in float32 would improve Cholesky conditioning significantly: a well-conditioned Gram matrix produces a more uniform gauge across bonds, which in turn reduces BP sweep count and eliminates most fallback events. The space cost is modest (only the gate workspace buffers double, not the full $O(\chi^2)$ state), and the timing cost is expected to be small because gate computation is arithmetic-bound in the L2-cache regime at $\chi \leq 100$. If fallbacks are eliminated, Adaptive QR would run strictly faster than Householder at $\chi = 100$, making it the unambiguous production mode for GPU-C across all grid sizes.